JOURNAL OF PETROLOGY | VOLUME 52 | NUMBER 2 | PAGES 401–430 | 2011 | doi:10.1093/petrology/egq085

Petrogenesis of Latest Miocene–Quaternary Continental Intraplate Volcanism along the Northern Dead Sea Fault System (Al Ghab–Homs Volcanic Field), Western Syria: Evidence for Lithosphere–Asthenosphere Interaction

GEORGE S.-K. MA[1]*, JOHN MALPAS[1], COSTAS XENOPHONTOS[1] AND GAVIN H.-N. CHAN[2]†

[1]DEPARTMENT OF EARTH SCIENCES, THE UNIVERSITY OF HONG KONG, POKFULAM ROAD, HONG KONG, CHINA
[2]DEPARTMENT OF EARTH SCIENCES, OXFORD UNIVERSITY, PARKS ROAD, OXFORD OX1 3PR, UK

RECEIVED MAY 8, 2009; ACCEPTED NOVEMBER 17, 2010
ADVANCE ACCESS PUBLICATION JANUARY 3, 2011

Late Miocene to Quaternary intraplate basaltic volcanism in the Al Ghab and Homs regions, northwestern Syria (the Al Ghab volcanic group and the Homs volcanic group), occurred roughly synchronously with the propagation of the Dead Sea Fault System in these regions. Petrographic evidence as well as major and trace element variations suggest that the basalts have undergone varying amounts of crystal fractionation of olivine ± clinopyroxene ± spinel, with feldspar fractionation only in the most evolved samples. The major and trace element chemistry and Nd–Sr–Pb isotopic variations of the basalts reflect both mantle source heterogeneity and relatively minor crustal contamination. Semi-quantitative assimilation–fractional crystallization modelling suggests that some samples may reflect assimilation of no more than 6% of upper continental crust, probably with Late Proterozoic Arabian Shield characteristics. Amongst the least crustally contaminated and relatively primitive samples, basanites are characterized by marked depletion of K, Rb and Zr relative to other neighbouring incompatible elements on primitive mantle normalized trace element diagrams. This, together with their low SiO_2 and high TiO_2 and Dy/Yb, is consistent with magma genesis involving a large proportion of garnet-bearing hornblendite or similar amphibole-rich metasomatic veins. Associated alkali and tholeiitic basalts with the higher SiO_2, lower TiO_2, less negative K, Rb and Zr anomalies, and moderately high Dy/Yb are consistent with melt extraction from a largely peridotitic mantle source. It is suggested that the compositional spectrum from basanite via alkali basalt to tholeiitic basalt can be explained by increasing degrees of metasomatic vein–wall-rock interaction, plus asthenospheric melt assimilation. In agreement with this is the identification of three distinct isotopic and chemical characteristics within the spectrum of mafic lavas, each of which can be referred to a unique mantle source (metasomatic vein, lithospheric wall-rock peridotite mantle and asthenospheric peridotite mantle). A decrease in eruption volume and increase in Si-undersaturation of the lavas from south (Homs) to north (Al Ghab) along the northern Dead Sea Fault System from latest Miocene to Quaternary times suggest a diminishing thermal perturbation and increasing importance of the amphibole-rich veins in magma genesis over time. It is proposed that the genesis of the oldest lavas reflects the arrival of asthenospheric melts beneath the Homs region, which with assimilation of lithospheric metasomatic veins and their wall-rocks produced the parental magmas of the Homs volcanic group. Subsequently, upwelling asthenospheric material could have been channelled northwards at the base of the lithosphere, presumably related to the northward propagation of the Dead Sea Fault System in the Pliocene. Cooling of this channelled asthenospheric material, which did not penetrate the lithosphere during this later period of magma genesis, provided the minimal thermal

*Corresponding author. Telephone: (852) 2857 8578. Fax: (852) 2517 6912. E-mail: georgema@graduate.hku.hk
†Present address: SRK Consulting, Level 2, 44 Market Street, Sydney, NSW 2000, Australia.

perturbation necessary for melting of amphibole-rich metasomatic veins and wall-rock peridotite within the lithosphere.

KEY WORDS: *amphibole: Dead Sea Fault System; intraplate volcanism: metasomatic veins; Nd–Sr–Pb isotopes*

INTRODUCTION

The origin of continental intraplate magmatism has been the focus of many petrological studies that have aimed to resolve the relative contributions of mantle plume material, asthenospheric mantle and lithospheric mantle in the genesis of magmas that compositionally have many affinities to ocean island basalts (OIB). In recent years, there has been increasing evidence that the source of intraplate magmas (the so-called OIB-source) contains mafic components in addition to peridotite (Niu & O'Hara, 2003; Kogiso *et al.*, 2004; Pilet *et al.*, 2004; Prytulak & Elliott, 2007). One possible model considers partial melting of a previously metasomatized lithospheric peridotite mantle source containing veins or pockets of pyroxenite and hornblendite, with or without interaction of the melts from sub-lithospheric mantle (plume or passively upwelling asthenosphere) (e.g. Bogaard & Wörner, 2003; Pilet *et al.*, 2008; Humphreys & Niu, 2009). In principle, partial melting of metasomatized peridotite, which will have a lower solidus temperature than anhydrous peridotite as a result of introduction of volatiles, hydrous phases or other heterogeneities (e.g. Katz *et al.*, 2003; Stolper & Asimow, 2007), can readily be achieved by lithospheric stretching (although less extensive than originally proposed by McKenzie & Bickle, 1988), as well as by heat conduction or advection by magmas derived from the underlying convecting mantle (McKenzie, 1989; Gallagher & Hawkesworth, 1992).

Although diverse opinions exist, there is increasing acceptance that the widespread Cenozoic intraplate alkaline volcanism in western Arabia involves partial melting of lithospheric mantle. Possible models proposed include melting of a 'fossilized' plume head (Stein & Hofmann, 1992; Stein & Goldstein, 1996) or of metasomatic veins (Weinstein *et al.*, 2006), which are now part of the lithosphere. Other models advocate mixing of lithospheric and asthenospheric melts (Shaw *et al.*, 2003, 2007; Lucassen *et al.*, 2008) or derivation from mainly mantle plume or asthenospheric sources (channelled plume material from the Afar plume; Camp & Roobol, 1992; Krienitz *et al.*, 2009), independent or 'pulsing' mantle plumes beneath single volcanic fields (Camp & Roobol, 1992; Krienitz *et al.*, 2007), passive upwelling of the shallow asthenosphere during times of extension or development of fault systems (Lustrino & Sharkov, 2006), and upper mantle upwelling induced by slab break-off along the Arabian–Turkish collision zone (Keskin, 2003; Krienitz *et al.*, 2006).

There are a number of scattered, small volcanic fields in the region that post-date or occurred synchronously with the development of the Dead Sea Fault System (DSFS), a sinistral fault system that has accommodated some 105 km (Freund *et al.*, 1970; Quennell, 1984) of movement since ~22–18 Ma (Bartov *et al.*, 1980; Eyal *et al.*, 1981) The 'propagation' of the northern segment of the DSFS into Syria did not commence until Pliocene times (Trifonov *et al.*, 1991; Brew *et al.*, 2001*b*). These volcanic fields have received little attention compared with the larger ones (e.g. Harrat Ash Shamah in Saudi Arabia, Jordan, Syria and the Golan Heights). Two are of latest Miocene–Early Pliocene (Homs volcanic field) and Late Pliocene–Quaternary (Al Ghab volcanic field) age and are located at step-overs of the DSFS in western Syria (Fig. 1). In this study we present evidence that the compositions of the erupted basalts can be explained in terms of partial melts derived from lithospheric metasomatic veins, their wall-rock peridotite and the upwelling asthenosphere. We attribute the cause of magma genesis to the arrival of upwelling asthenospheric material beneath the Homs region for the older volcanism and northward migration of this material along the base of the lithosphere for the younger volcanism in Al Ghab.

The Homs volcanic field

The Homs volcanic field covers ~500 km^2 and is mainly composed of alkali and tholeiitic basalts (Fig. 1). The latest Miocene–Early Pliocene age of the volcanic field is well constrained by $^{40}Ar/^{39}Ar$ dates of between 6·4 and 3·7 Ma at the base and top of the lava pile at Krak des Chevaliers (Searle *et al.*, 2010). The Homs volcanic field consists of lava flows with minor pyroclastic deposits, and is associated with the 1000 m high Shin shield volcano.

The Al Ghab volcanic field

In contrast to the Homs volcanic field, volcanic rocks in northern Al Ghab are associated with numerous minor cinder cones that have produced lava flows and scoriaceous materials covering only relatively small areas (Fig. 1). Single lava fields usually do not exceed 25 km^2 in extent and 20 m thickness, and involve several cinder cones. The lavas have been dated by K/Ar and $^{40}Ar/^{39}Ar$ methods at 4·0–1·1 Ma, with the vast majority younger than 2 Ma (Sharkov *et al.*, 1994, 1998; Krienitz *et al.*, 2009; Searle *et al.*, 2010). There are some 40 cinder and lava cones within an area of 600 km^2 in northern Al Ghab, and several contain spinel peridotite xenoliths (and minor pyroxenite, hornblendite and lower crustal fragments). In the following discussion, unless specifically stated, the latest Miocene–Quaternary volcanic rocks in the region of the Al Ghab depression and Homs are collectively termed northern Dead Sea Fault System (N-DSFS) volcanic rocks.

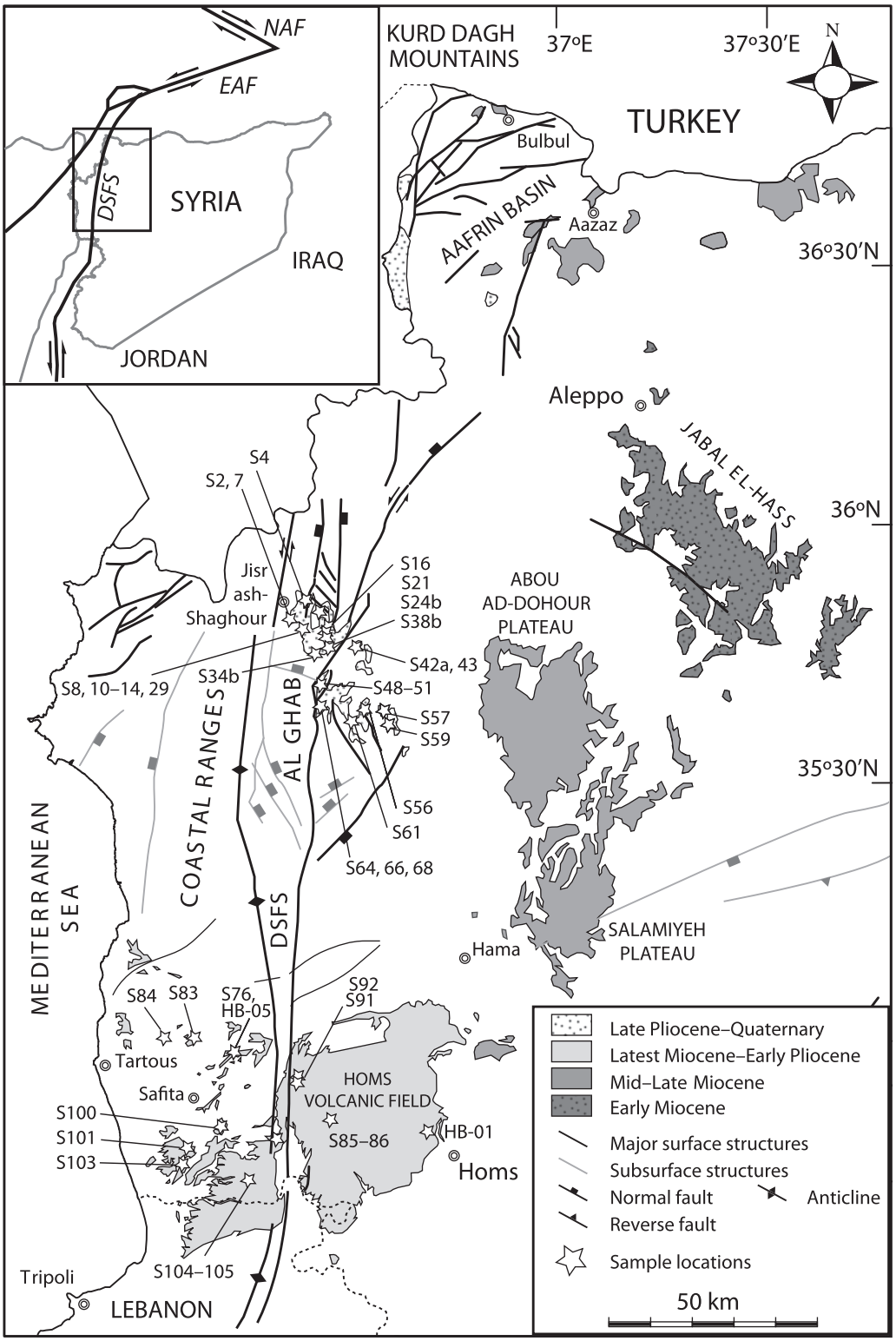

Fig. 1. Distribution of Cenozoic volcanic rocks in northwestern Syria and northern Lebanon, with major structural features redrawn after Brew *et al.* (2001*a*). Sampling locations are marked by star symbols (with sample numbers). EAF, East Anatolian Fault; NAF, North Anatolian Fault; DSFS, Dead Sea Fault System.

SAMPLE DESCRIPTION AND MINERAL CHEMISTRY

The Homs volcanic group comprises basanites, alkali basalts and tholeiitic basalts, whereas the Al Ghab volcanic group comprises mainly basanites and subordinate amounts of hawaiite and alkali basalt, based on the classification of Le Maitre (2002) (Fig. 2). Representative bulk-rock major and trace element compositions are reported in Table 1. Descriptions of the sampling strategy and analytical methods are given in Appendix A. In Fig. 2, fields of recently published data (Abdel-Rahman & Nassar, 2004; Lustrino & Sharkov, 2006; Krienitz *et al.*, 2009) (Appendix B) from the same study area are also shown for comparison with the results of this study, except for one evolved lava (3·1 wt % MgO; Krienitz *et al.*, 2009).

The N-DSFS lavas are porphyritic with up to ~20 vol. % euhedral to subhedral phenocrysts of ~0·5–9 mm diameter, scattered in a microcrystalline, or rarely cryptocrystalline, groundmass of plagioclase, clinopyroxene, olivine and Fe–Ti oxides. Trachytic textures are common. Intergranular and rarely sub-ophitic textures are observed in somewhat coarser-grained samples. Phenocryst phases are predominantly olivine (5–15 vol. %) ± clinopyroxene (<5 vol. %) ± plagioclase (<5 vol. %) ± opaque minerals (<2 vol. %). No correlation is observed between phenocryst populations and magma type, although plagioclase phenocrysts tend to be more common in samples with low MgO (<6·5 wt %). Representative electron microprobe analyses of the constituent minerals are given in Table 2. The complete dataset (Electronic Appendix 1) is available at http://www.petrology.oxfordjournals.org/.

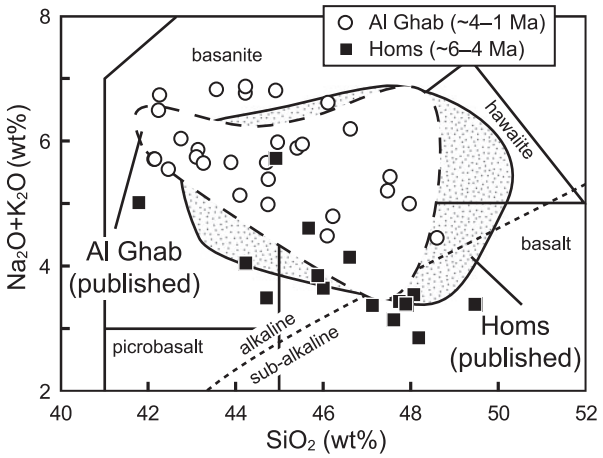

Fig. 2. Total alkalis vs silica diagram of Le Maitre (2002). The alkaline–sub-alkaline divide is from Irvine & Baragar (1971). The dashed (northern Al Ghab) and continuous (Homs) lines represent the range of compositions reported in the literature (Abdel-Rahman & Nassar, 2004; Lustrino & Sharkov, 2006; Krienitz *et al.*, 2009).

The olivine phenocrysts are typically euhedral to subhedral, up to ~9 mm (in S92-05; mostly ~1–2 mm) and in places embayed (less common for micro-phenocrysts), with rims commonly replaced by yellowish to reddish brown iddingsite. Forsterite contents are $Fo_{60–89}$ for the phenocrysts (including micro-phenocrysts), and $Fo_{52–55}$ for the groundmass. Micro-phenocrysts tend to have lower Fo contents than the larger, euhedral ones, approaching those of the groundmass. Most of the olivine phenocrysts display normal compositional zoning, generally with a <15% decrease in Fo content from core to rim (Fig. 3). Some of the cores contain small Cr-spinel inclusions (Cr-number = 16·7–55·3). The phenocryst as well as groundmass compositions are summarized in Fig. 3 on a plot of forsterite content vs bulk-rock Mg-number [Mg-number = $100 \times Mg/(Mg + Fe^{2+})$]. It appears that most of the phenocryst cores from the relatively primitive volcanic rocks (Mg-number > 55) approach equilibrium with their bulk-rock compositions, using a $K_D^{ol/Liq}{}_{Fe–Mg}$ between 0·27 and 0·33 (Roeder & Emslie, 1970), although some outliers exist, most of which are those in S76-05 (Mg-number = 59), which has forsterite contents up to Fo_{89}. These disequilibrium olivines are characterized by euhedral shapes (with or without embayments), high CaO contents (≥0·13 wt %, except for one Fo_{80} core that has 0·05 wt % CaO); higher than those of mantle olivines, which generally have <0·1 wt % CaO (Thompson & Gibson, 2000) and lack signs of deformation (e.g. kink-bands), suggesting that they are probably intratelluric crystals that crystallized earlier from a more primitive magma and were subsequently incorporated into a more evolved magma, rather than being xenocrysts of lithospheric mantle origin.

The most forsteritic olivine cores from the relatively evolved lavas (Mg-number < 55) are not in equilibrium (too forsteritic) with their bulk-rock compositions. These lavas, particularly S49-05b and S48-05 (the lowest-Mg-number samples in Fig. 3), also contain abundant clinopyroxene and plagioclase phenocrysts. The Mg-numbers of these rocks have probably been affected by fractionation and/or accumulation of clinopyroxene ± plagioclase ± olivine.

Of the ~100 lava, scoria and bomb samples collected, approximately one-third are clinopyroxene-phyric. The clinopyroxene phenocrysts are typically <5 vol. % (up to ~10 vol. %) and commonly form glomerocrysts together with olivine and plagioclase. The majority are diopside, but some are augite, following the classification of Morimoto (1989), with the groundmass clinopyroxenes typically having higher wollastonite contents (groundmass $Wo_{47–51}En_{33–39}$ vs phenocrysts $Wo_{44–51}En_{33–44}$). Compared with the large phenocrysts, the smaller micro-phenocrysts are compositionally more akin to clinopyroxenes in the groundmass, characterized by higher Ti and Al values.

Table 1: Major (wt %) and trace element (ppm) data of northern DSFS basalts analysed in this study

Sample:	S2-05	S4-05	S7-05	S8-05	S10-05	S11-05	S12-05	S13-05	S14-05	S16-05	S21-05	S23-05	S24-05b	S29-05	S34-05	S38-05b
Lat. (°N):	35°46′16″	35°49′42″	35°46′33″	35°46′02″	35°46′02″	35°46′02″	35°46′10″	35°46′10″	35°46′10″	35°46′18″	35°45′40″	35°48′16″	35°44′34″	35°46′21″	35°42′49″	35°43′55″
Long. (°E):	36°18′43″	36°20′21″	36°19′11″	36°21′29″	36°21′29″	36°21′29″	36°21′23″	36°21′23″	36°21′23″	36°23′38″	36°24′26″	36°23′45″	36°24′55″	36°21′53″	36°24′18″	36°25′52″
Province:	AG	AG	AG	AG	AG	AG	AG	AG	AG	AG	AG	AG	AG	AG	AG	AG
Rock type:	Bas	Bas	Bas	Bas	Bas	Bas	Bas	Bas	Bas	Bas	Bas	Bas	Bas	Bas	Bas	Bas
SiO_2	42·43	41·92	43·24	41·63	40·77	43·28	41·63	40·87	40·67	45·06	40·57	41·95	45·24	41·41	42·74	43·70
TiO_2	3·34	3·60	3·03	3·22	3·62	2·88	3·13	4·01	4·13	3·05	3·00	2·93	2·96	3·46	2·85	3·51
Al_2O_3	13·16	13·46	13·37	13·19	12·78	13·51	12·97	13·23	13·40	14·12	12·94	13·35	14·02	12·96	13·36	13·99
Fe_2O_3	13·51	13·43	13·69	14·16	13·30	13·34	13·84	13·53	13·75	13·76	14·26	13·54	13·89	14·90	12·82	14·18
MnO	0·16	0·16	0·18	0·18	0·15	0·18	0·18	0·17	0·17	0·18	0·20	0·19	0·19	0·20	0·17	0·18
MgO	7·08	8·58	9·25	8·39	10·06	8·58	8·17	8·10	7·17	6·96	7·96	7·29	6·60	7·18	7·87	6·37
CaO	9·96	9·96	10·12	10·00	10·52	9·66	10·39	10·13	9·91	8·57	11·10	10·85	8·54	10·83	9·21	9·19
Na_2O	4·35	3·92	3·89	4·44	3·84	3·58	4·48	5·22	5·19	4·63	4·51	3·99	3·92	4·98	4·41	4·80
K_2O	2·13	1·77	1·68	1·10	1·68	1·63	0·95	1·05	1·28	1·82	0·98	0·89	2·08	0·86	1·27	0·86
P_2O_5	1·16	1·69	1·41	1·66	1·35	1·40	1·84	1·78	1·91	0·94	2·12	1·49	0·97	1·54	1·63	0·87
LOI	2·50	0·13	gain	1·50	0·74	1·23	2·03	0·87	1·18	0·40	1·87	3·36	1·13	1·80	3·00	2·03
Total	99·80	98·60	99·90	99·50	98·80	99·30	99·60	99·00	98·80	99·50	99·50	99·80	99·50	100·10	99·30	99·70
Mg-no.	53·6	58·4	59·8	56·6	62·5	58·6	56·5	56·9	53·4	52·7	55·1	54·2	51·1	51·5	57·5	49·7
Sc	14·4	18·0	20·2	16·1	18·8	15·9	15·4	19·6	14·1	12·7	14·7	12·9	13·2	13·8	13·5	13·9
V	174	210	215	222	180	184	211	206	198	152	176	197	174	181	177	181
Cr	134	268	158	189	169	182	157	156	145	103	177	171	94	130	156	110
Ni	–	–	–	–	156	195	–	178	–	81	–	–	–	–	–	–
Cu	–	–	–	–	–	26·0	–	21·0	–	–	–	–	–	–	–	–
Zn	121	123	119	122	123	113	121	126	140	115	124	107	138	124	114	125
Ga	25	22	23	23	23	22	23	24	25	21	22	19	25	23	22	24
Rb	33·5	18·2	27·8	23·2	28·2	21·7	17·4	19·2	15·4	17·7	7·7	15·7	25·4	24·3	24·7	9·2
Sr	1579	1254	1465	1300	1635	1387	1854	1740	1977	857	1766	1336	1061	1337	1310	932
Y	25·0	24·4	26·7	27·4	27·9	26·2	28·6	28·1	28·8	21·1	28·7	23·5	24·8	29·6	25·7	23·0
Zr	296	241	230	265	261	195	256	276	307	255	275	256	292	278	243	279
Nb	85·8	81·4	72·5	81·5	84·9	75·5	85·6	88·9	101·0	57·0	94·3	75·4	66·4	90·8	75·8	61·8
Ba	638	504	618	585	701	545	606	692	658	295		490	373	575	549	458
La	62·0	63·4	72·4	82·2	87·3	73·6	89·6	89·8	93·3	38·1	89·7	61·6	50·1	71·4	76·7	43·9
Ce	122	122	141	166	166	122	152	171	177	78·8	149	121	110	143	135	72·8
Pr	14·0	13·9	15·3	17·5	18·7	14·8	18·4	19·5	20·2	9·47	19·0	13·9	12·5	14·8	15·9	10·6
Nd	56·6	50·2	58·8	69·5	67·9	58·8	72·2	70·4	73·0	36·1	77·6	49·4	46·8	60·6	63·2	39·3
Sm	10·9	9·78	10·5	12·9	11·7	11·0	13·4	12·4	13·1	7·54	14·0	9·36	9·63	12·1	11·8	8·54
Eu	3·66	3·00	3·34	3·84	3·65	3·48	4·02	3·76	4·00	2·50	4·51	2·88	3·08	3·80	3·57	2·74
Gd	10·3	8·58	9·51	9·93	10·1	9·02	10·1	10·4	11·0	6·28	11·5	7·58	7·49	9·90	9·22	7·14
Tb	1·24	1·09	1·22	1·31	1·30	1·21	1·39	1·33	1·32	0·87	1·47	1·01	1·08	1·38	1·26	1·02
Dy	5·88	5·40	5·98	6·45	6·24	6·05	6·86	6·53	6·44	4·47	7·27	4·91	5·54	6·78	6·08	5·02
Ho	1·03	0·95	0·97	1·12	1·02	1·06	1·19	1·07	1·07	0·79	1·25	0·85	0·97	1·17	1·03	0·87
Er	2·50	2·26	2·37	2·62	2·52	2·56	2·78	2·57	2·61	1·88	2·95	2·11	2·27	2·76	2·41	2·08
Tm	0·27	0·28	0·29	0·32	0·30	0·32	0·35	0·30	0·29	0·24	0·37	0·27	0·28	0·35	0·31	0·27
Yb	1·61	1·51	1·78	1·79	1·77	1·85	1·95	1·80	1·67	1·30	2·09	1·49	1·57	1·95	1·72	1·55
Lu	0·22	0·24	0·28	0·24	0·24	0·26	0·26	0·26	0·23	0·19	0·28	0·20	0·21	0·26	0·24	0·21
Hf	6·35	4·96	4·94	6·44	5·47	5·78	6·36	5·67	6·14	5·48	7·08	5·23	7·73	6·80	6·20	6·69
Ta	5·03	4·43	4·13	5·20	4·58	4·64	5·42	4·81	5·27	3·97	6·36	4·19	5·40	6·06	5·01	4·53
Pb	3·59	3·24	3·83	3·87	4·66	4·07	4·41	4·44	4·81	2·96	4·30	3·17	3·67	3·99	4·12	2·86
Th	5·61	5·98	5·99	7·11	7·48	7·03	8·07	7·65	8·01	4·39	8·02	5·53	6·01	7·93	7·78	4·70
U	1·73	1·70	1·80	2·16	2·05	2·04	2·43	2·13	2·30	1·37	2·25	1·64	1·94	2·30	2·30	1·46

(continued)

Table 1: Continued

Sample:	S42-05a	S43-05	S48-05	S49-05b	S50-05	S51-05	S56-05	S57-05	S59-05	S61-05	S64-05	S66-05	S68-05	S76-05	S83-05	S84-05
Lat. (°N):	35°43′54″	35°43′47″	35°37′48″	35°38′58″	35°39′33″	35°38′29″	35°36′26″	35°36′24″	35°34′38″	35°34′41″	35°36′29″	35°36′29″	35°36′28″	34°55′51″	34°57′33″	34°57′23″
Long. (°E):	36°28′53″	36°29′02″	36°23′35″	36°23′17″	36°24′28″	36°25′03″	36°30′34″	36°32′23″	36°33′04″	36°27′59″	36°24′00″	36°24′00″	36°24′05″	36°10′23″	36°06′14″	36°02′47″
Province:	AG	AG	AG	AG	AG	AG	AG	AG	AG	AG	AG	AG	AG	Homs	Homs	Homs
Rock type:	Bas	Bas	AB	Haw	AB	Haw	Bas	AB	AB	Bas	Bas	Bas	Bas	Bas	AB	TB
SiO_2	42·94	43·44	47·70	46·85	46·78	46·28	40·89	44·34	44·19	43·09	42·00	43·30	43·44	40·26	44·13	46·11
TiO_2	4·32	3·27	2·70	3·22	2·72	3·07	2·77	2·43	2·23	3·23	4·02	4·06	2·83	3·36	3·12	2·07
Al_2O_3	14·25	13·77	14·60	15·62	15·63	14·97	12·88	13·08	13·33	13·95	13·74	13·92	13·39	13·36	14·49	14·68
Fe_2O_3	13·88	13·85	13·05	12·87	12·89	12·97	13·50	13·23	12·67	13·77	13·02	13·47	13·05	14·04	13·59	14·40
MnO	0·17	0·17	0·16	0·15	0·16	0·15	0·18	0·18	0·17	0·17	0·16	0·16	0·17	0·19	0·17	0·17
MgO	6·31	6·32	6·65	5·69	5·70	6·13	9·06	8·29	8·26	7·26	7·19	6·69	9·11	9·14	7·12	7·63
CaO	9·06	9·45	9·55	9·49	9·38	9·47	11·11	10·59	11·55	10·44	9·68	8·74	9·81	10·92	10·19	9·03
Na_2O	5·54	4·63	3·35	4·18	3·79	3·96	4·55	3·47	3·31	3·96	5·39	5·15	3·83	4·04	3·35	2·13
K_2O	1·12	1·04	1·02	1·17	1·08	1·11	0·79	1·13	0·99	0·84	1·18	1·40	1·66	0·79	1·10	0·61
P_2O_5	0·87	0·86	0·67	0·61	0·67	0·67	1·89	0·50	0·42	0·97	1·32	0·84	1·16	1·62	0·72	0·30
LOI	1·27	2·61	gain	gain	0·37	0·17	1·73	2·06	2·27	1·21	0·95	0·91	0·30	1·92	1·43	1·65
Total	99·70	99·40	99·50	99·60	99·20	98·90	99·40	99·30	99·40	98·90	98·60	98·60	98·80	99·60	99·40	98·80
Mg-no.	50·0	50·1	52·9	49·3	49·3	51·0	59·6	58·0	58·9	53·7	54·9	52·2	60·6	58·9	53·6	53·8
Sc	20·9	15·2	16·4	16·8	17·0	19·0	17·6	17·0	15·8	15·7	18·6	17·5	16·5	15·7	19·0	23·2
V	242	206	201	123	138	198	206	209	181	141	196	205	212	208	203	208
Cr	140	128	190	120	127	169	235	245	255	141	139	126	202	142	124	278
Ni	143	–	–	67	–	–	–	–	233	–	147	–	204	148	–	–
Cu	12·0	–	–	22·0	–	–	–	–	45·0	–	15·0	–	30·0	23·0	–	–
Zn	143	133	105	107	111	109	117	112	95·0	115	127	125	113	130	91·0	99·0
Ga	27	25	22	23	24	22	22	23	18	22	25	25	22	23	20	18
Rb	45·7	25·1	13·7	15·0	14·4	17·2	4·6	15·4	12·0	5·1	39·6	17·4	22·0	16·0	10·7	7·1
Sr	1179	1032	726	741	752	770	1244	638	514	936	1352	997	1298	1505	776	353
Y	27·5	25·1	21·8	23·1	23·1	21·7	29·1	20·9	16·6	24·1	27·2	24·1	24·7	27·3	25·1	20·6
Zr	317	277	164	174	188	166	249	189	138	232	282	278	212	284	196	101
Nb	74·0	65·7	44·9	44·9	45·7	43·5	92·1	39·4	28·7	55·8	80·8	64·1	62·4	106·0	47·3	16·7
Ba	472	373	265	292	261	365	649	335	295	403	626	412	451	653	247	122
La	49·8	45·4	29·8	28·4	27·9	33·0	91·9	25·9	19·7	46·0	67·4	47·4	54·2	86·3	30·0	12·2
Ce	103·0	90·6	60·9	58·7	60·2	66·1	154	55·1	40·1	90·5	131	93·4	107	153	65·6	25·8
Pr	12·4	11·5	7·65	7·62	7·62	7·72	18·7	6·78	4·94	10·9	14·9	11·1	12·5	18·6	8·28	3·42
Nd	47·7	42·5	29·1	29·5	29·2	31·0	71·5	26·3	19·4	40·0	58·3	44·8	46·4	66·4	29·8	14·9
Sm	9·70	9·08	6·49	6·55	6·56	6·56	13·1	6·07	4·66	8·39	11·2	8·83	9·28	12·9	6·17	3·77
Eu	3·10	2·91	2·15	2·22	2·27	2·16	3·92	1·93	1·56	2·72	3·47	2·98	2·91	3·65	2·18	1·34
Gd	8·84	7·24	5·45	5·79	5·87	6·10	10·4	5·40	4·35	7·28	9·42	8·04	7·63	10·4	6·58	4·43
Tb	1·16	1·06	0·84	0·89	0·86	0·80	1·40	0·81	0·61	1·03	1·23	1·03	1·08	1·32	0·90	0·61
Dy	5·89	5·45	4·47	4·75	4·79	4·24	6·89	4·44	3·47	5·12	6·01	5·29	5·33	6·27	4·52	3·35
Ho	0·99	0·95	0·81	0·86	0·86	0·80	1·19	0·79	0·62	0·88	1·00	0·90	0·93	1·06	0·87	0·72
Er	2·37	2·22	1·97	2·14	2·17	2·14	2·77	1·88	1·51	2·16	2·45	2·25	2·20	2·57	2·21	1·83
Tm	0·28	0·28	0·27	0·28	0·28	0·25	0·35	0·24	0·20	0·28	0·29	0·26	0·29	0·32	0·28	0·25
Yb	1·62	1·60	1·55	1·65	1·66	1·55	1·99	1·43	1·25	1·61	1·68	1·50	1·64	1·65	1·50	1·51
Lu	0·23	0·22	0·21	0·23	0·23	0·23	0·29	0·21	0·16	0·21	0·24	0·20	0·24	0·25	0·21	0·20
Hf	6·81	6·88	4·18	4·68	4·67	4·05	6·45	4·83	3·63	5·46	6·02	5·93	5·32	5·93	3·97	2·14
Ta	5·21	4·91	2·86	2·95	2·98	2·71	5·66	2·80	2·10	3·53	4·90	4·69	3·99	5·55	2·63	0·90
Pb	3·16	2·87	1·94	1·74	1·83	2·80	4·53	2·85	2·19	2·59	4·14	3·57	3·05	4·37	2·03	0·86
Th	4·79	4·19	2·90	2·62	2·63	3·08	9·17	3·00	2·22	4·21	7·10	5·62	4·87	8·17	2·40	1·42
U	1·42	1·36	0·86	0·79	0·83	0·86	2·58	0·92	0·64	1·15	1·97	1·57	1·46	2·94	0·83	0·39

(continued)

Table 1: Continued

Sample:	S85-05	S86-05	S91-05	S92-05	S97-05	S100-05	S101-05	S103-05	S104-05	S105-05	HB-01	HB-05	AGV-2	BHVO-2	GSR-3
Lat. (°N):	34°46′17″	34°48′02″	34°52′16″	34°53′22″	34°45′26″	34°46′49″	34°44′18″	34°42′31″	34°40′47″	34°40′44″	34°46′02″	34°55′45″			
Long. (°E):	36°25′57″	36°24′35″	36°20′32″	36°20′22″	36°17′44″	36°09′51″	36°04′59″	36°04′15″	36°13′17″	36°14′01″	36°40′43″	36°12′22″			
Province:	Homs	Homs	Homs	Homs	Homs	Homs	Homs	Homs	Homs	Homs	Homs	Homs	Ref. mat.	Ref. mat.	Ref. mat.
Rock type:	Bas	AB	AB	Bas	AB	TB	TB	TB	TB	TB	TB	Bas	$n=1$	$n=3$	$n=2$
SiO_2	42·76	45·36	45·01	43·54	45·31	45·77	46·56	46·51	47·64	45·78	46·45	43·97	59·01	49·4	44·74
TiO_2	3·81	2·58	2·39	2·38	2·45	1·96	2·36	2·54	1·96	2·17	2·32	3·74	1·07	2·8	2·35
Al_2O_3	14·50	14·49	14·00	13·18	13·78	15·24	15·80	14·53	14·48	13·25	15·45	15·41	17·01	13·4	13·9
Fe_2O_3	14·30	14·73	13·40	14·17	13·87	13·58	13·64	14·04	13·34	14·72	13·26	14·77	6·77	12·5	13·34
MnO	0·15	0·18	0·18	0·19	0·17	0·17	0·16	0·17	0·17	0·10	0·07	0·07	0·10	0·16	0·14
MgO	7·14	9·32	9·96	11·36	8·97	7·36	5·62	8·20	7·50	9·57	7·28	6·16	1·53	7·13	7·8
CaO	10·47	9·24	10·14	9·83	9·27	9·31	10·29	9·51	8·98	9·21	9·81	8·37	5·01	11·32	8·8
Na_2O	2·75	2·76	2·96	2·55	2·91	2·62	2·81	2·50	2·59	2·47	2·59	4·17	4·34	2·2	3·30
K_2O	1·17	0·84	0·82	0·86	1·12	0·68	0·63	0·58	0·68	0·82	0·71	1·42	2·94	0·53	2·3
P_2O_5	1·03	0·55	0·58	0·73	0·74	0·52	0·35	0·50	0·30	0·52	0·37	1·26	0·52	0·258	0·96
LOI	0·91	gain	0·07	gain	1·07	1·47	1·37	0·91	1·90	gain	0·07	gain	2·6		
Total	99·00	100·10	99·50	98·80	99·70	98·70	99·60	100·00	99·50	98·61	98·38	99·34	98·29	99·68	100·23
Mg-no.	52·4	58·2	62·1	63·8	58·7	54·4	47·6	56·3	55·3	58·9	54·7	47·9			
													$n=4$	$n=5$	$n=3$
Sc	21·0	22·0	26·9	20·2	23·2	18·8	23·7	20·5	21·4	21·9	26·2	19·0	13·2	29	15·1
V	244	201	243	178	221	179	263	205	189	203	237	249	118	320	164·5
Cr	179	273	446	283	301	284	253	226	259	344	232	36·7	17	293	139
Ni	121	199	–	360	244	–	113	149	242	226	92·0	63·0	–	124	–
Cu	58·0	68·0	–	47·0	36·0	–	57·0	47·0	47·0	49·0	39·0	33·0	–	119	–
Zn	127	116	107	88·0	127	96·9	110	102	99·0	102	103	121	91	29	141
Ga	23	22	21	17	23	21	22	17	18	21	23	24	20·1	320	24·9
Rb	14·8	11·6	7·17	8·13	13·7	8·94	8·30	9·70	8·11	9·83	7·66	12·5	71	293	42
Sr	1033	578	653	675	829	540	526	560	398	591	439	1204	638	113	1103
Y	34·0	23·2	24·2	19·1	25·1	27·8	24·7	21·6	22·1	20·4	23·4	28·2	19·9	21	22·8
Zr	215	149	166	145	177	129	116	158	126	131	133	222	228	9·7	276
Nb	59·1	34·2	26·8	37·9	43·2	25·8	15·9	22·5	16·0	29·6	21·6	59·8	14·1	382	72
Ba	541	238	186	231	311	310	150	135	135	238	197	440	1141	25·5	578
La	53·8	28·2	27·5	27·4	39·1	29·0	14·3	18·9	11·8	21·8	15·2	57·0	40	168	57
Ce	103	61·1	53·2	58·0	73·7	51·0	32·0	41·6	26·8	45·6	34·2	106	72	17·9	109·4
Pr	14·0	7·39	6·77	7·34	9·07	6·38	4·28	5·30	3·84	5·68	4·70	12·1	8·4	137	12·7
Nd	55·5	29·9	27·9	28·1	36·4	26·2	18·6	22·1	16·1	24·0	20·4	46·6	30	15	50
Sm	11·2	6·35	5·90	5·37	7·26	5·99	4·81	5·70	4·30	5·47	5·17	9·29	5·6	38	10·4
Eu	3·50	2·10	2·02	1·65	2·39	1·99	1·67	1·78	1·37	1·98	1·84	3·12	1·5	5·3	3·2
Gd	9·77	6·23	5·76	5·13	6·78	6·17	4·90	5·60	4·56	5·61	5·55	9·65	4·8	24	9·1
Tb	1·34	0·90	0·90	0·79	0·98	0·89	0·76	0·77	0·71	0·82	0·85	1·20	0·66	6·1	1·16
Dy	7·02	5·01	4·82	3·66	5·25	5·06	4·51	4·42	3·92	4·14	4·40	5·62	3·5	2·0	5·45
Ho	1·14	0·89	0·91	0·72	0·90	1·02	0·88	0·86	0·80	0·82	0·90	1·10	0·67	6·2	0·89
Er	2·98	2·33	2·23	1·68	2·26	2·56	2·17	1·97	2·00	1·98	2·34	2·70	1·84	0·94	2·01
Tm	0·36	0·30	0·30	0·24	0·28	0·33	0·29	0·27	0·28	0·25	0·31	0·34	0·256	5·2	0·214
Yb	2·19	1·79	1·86	1·34	1·70	1·98	1·75	1·58	1·58	1·60	1·92	2·04	1·61	1·01	1·18
Lu	0·31	0·26	0·24	0·18	0·23	0·28	0·26	0·22	0·21	0·22	0·26	0·27	0·25	2·5	0·157
Hf	4·72	3·67	3·61	3·42	3·92	3·35	3·25	3·35	3·15	3·11	3·07	4·41	5·0	0·33	5·94
Ta	3·56	2·51	1·92	2·35	2·45	1·69	1·32	1·35	1·15	1·67	1·24	2·83	0·83	1·9	4·2
Pb	2·61	1·85	1·20	1·41	2·98	1·57	1·18	1·13	1·04	1·58	1·56	2·59	13·3	0·28	4·9
Th	4·10	2·31	2·22	2·84	3·30	2·41	1·13	1·40	1·33	1·92	1·29	4·35	6·1	4·1	5·8
U	1·07	0·63	0·67	0·83	0·96	0·44	0·33	0·41	0·33	0·58	0·38	1·43	1·9	1·1	1·41

Bulk-rock Mg-number = mol % $Mg/(Mg+Fe^{2+})$ assuming 10% total Fe as Fe_2O_3; LOI, loss on ignition; –, data not available; AG, Al Ghab volcanic group; Homs, Homs volcanic group; AB, alkali basalt; Bas, basanite; Haw, hawaiite; TB, tholeiitic basalt.

Table 2: Representative electron microprobe analyses (wt %) of minerals from the N-DSFS lavas

Sample	Lab. no.	Comment	SiO_2	TiO_2	Al_2O_3	Fe_2O_3*	FeO	MnO	MgO	CaO	Na_2O	K_2O	Cr_2O_3	NiO	Total	Mg-no.	Cr-no.	An (En)	Ab (Fs)	Or (Wo)
Olivines																				
S7-05	S7__GZ27	core	39·29	b.d.l.	0·05	–	17·33	0·27	42·46	0·23	b.d.l.	0·03	b.d.l.	0·23	99·91	81·4	–	–	–	–
S7-05	S7__GZ28	rim of S7__GZ28	37·11	b.d.l.	0·05	–	31·33	0·71	30·55	0·46	b.d.l.	0·02	b.d.l.	b.d.l.	100·24	63·5	–	–	–	–
S48-05	S48__GZ10	core (glomerocryst)	39·81	b.d.l.	0·06	–	17·26	0·24	42·86	0·19	b.d.l.	b.d.l.	b.d.l.	0·13	100·55	81·6	–	–	–	–
S48-05	S48__GZ11	rim of S48__GZ10	38·76	b.d.l.	0·04	–	22·25	0·39	38·00	0·24	b.d.l.	b.d.l.	b.d.l.	b.d.l.	99·70	75·3	–	–	–	–
S49-05b	S49b__GZ42	groundmass	34·65	0·13	0·05	–	40·19	0·75	23·99	0·48	0·04	0·03	b.d.l.	b.d.l.	100·30	51·5	–	–	–	–
S49-05b	S49b__GZ29	core	38·58	b.d.l.	b.d.l.	–	19·24	0·24	41·59	0·21	b.d.l.	b.d.l.	0·09	0·15	100·11	79·4	–	–	–	–
S49-05b	S49b__GZ30	rim of S49b__GZ29	39·07	b.d.l.	0·05	–	21·83	0·26	38·91	0·29	0·06	0·03	b.d.l.	b.d.l.	100·49	76·1	–	–	–	–
S76-05	S76__GZ01	core	40·78	b.d.l.	0·10	–	10·39	0·21	47·97	0·18	b.d.l.	b.d.l.	b.d.l.	0·34	99·96	89·2	–	–	–	–
S76-05	S76__GZ02	rim of S76__GZ01	39·19	b.d.l.	0·04	–	22·41	0·54	37·49	0·29	0·04	b.d.l.	b.d.l.	b.d.l.	99·98	74·9	–	–	–	–
S91-05	S91__GZ27	core	40·41	b.d.l.	b.d.l.	–	15·53	0·16	43·39	0·21	b.d.l.	b.d.l.	b.d.l.	0·21	99·92	83·3	–	–	–	–
S91-05	S91__GZ28	rim of S91__GZ17	38·67	b.d.l.	b.d.l.	–	23·48	0·59	36·81	0·28	b.d.l.	b.d.l.	b.d.l.	b.d.l.	99·82	73·6	–	–	–	–
S92-05	S92__GZ14	core	40·38	b.d.l.	0·06	–	13·59	0·18	45·23	0·19	0·07	b.d.l.	b.d.l.	0·16	99·85	85·6	–	–	–	–
S92-05	S92__GZ15	rim of S92__GZ14	38·88	b.d.l.	0·05	–	15·50	0·15	44·17	0·21	0·07	b.d.l.	b.d.l.	0·28	99·30	83·5	–	–	–	–
Clinopyroxenes																				
S49-05b	S49b__GZ21	core	50·70	0·84	5·14	–	6·88	0·08	14·68	20·88	0·56	b.d.l.	0·49	b.d.l.	100·25	79·2	–	43·7	11·6	44·7
S49-05b	S49b__GZ22	rim of S49b__GZ21	48·45	1·16	6·76	–	7·25	0·09	13·18	21·57	0·59	b.d.l.	0·34	b.d.l.	99·39	76·4	–	40·2	12·6	47·3
S68-05	S68__GZ05	core (micro-phenocryst)	42·54	3·15	10·40	–	8·93	0·13	10·82	22·94	0·45	0·02	b.d.l.	b.d.l.	99·39	68·4	–	33·4	15·7	50·9
S68-05	S68__GZ16	groundmass	44·39	3·10	8·71	–	8·68	0·17	10·71	22·73	0·51	0·04	b.d.l.	0·16	99·19	68·7	–	33·4	15·5	51·0
S76-05	S76__GZ30	groundmass	46·77	2·38	5·83	–	7·18	0·22	12·24	23·77	0·73	0·03	b.d.l.	b.d.l.	99·16	75·2	–	36·6	12·4	51·0
S92-05	S92__GZ18	core	48·73	1·40	6·58	–	8·39	0·17	12·24	22·01	1·06	b.d.l.	b.d.l.	b.d.l.	100·56	72·2	–	37·2	14·6	48·1
S92-05	S92__GZ19	rim of S92__GZ18	48·96	1·31	6·35	–	8·25	0·22	12·51	21·97	1·03	0·02	b.d.l.	b.d.l.	100·62	73·0	–	37·8	14·4	47·8
S92-05	S92__GZ20	inclusion in S92__GZ18	47·43	1·88	5·37	–	7·91	0·15	12·61	23·15	0·67	b.d.l.	b.d.l.	b.d.l.	99·16	74·0	–	37·3	13·4	49·3
Feldspars																				
S48-05	S48__GZ16	phenocryst core	53·16	0·12	29·14	–	0·71	b.d.l.	b.d.l.	12·83	4·43	0·31	n.a.	b.d.l.	100·69	–	–	60·5	37·8	1·8
S48-05	S48__GZ39	groundmass	55·56	0·19	27·24	–	0·88	b.d.l.	b.d.l.	10·45	5·73	0·48	n.a.	b.d.l.	100·51	–	–	48·9	48·5	2·6
S49-05b	S49b__GZ34	phenocryst	52·29	0·15	28·91	–	0·54	b.d.l.	0·06	12·90	4·29	0·23	n.a.	b.d.l.	99·36	–	–	61·6	37·0	1·3
S73-05d†		megacryst ($n=8$)	67·25	–	19·98	–	0·18	–	–	0·48	8·68	3·37	n.a.	–	99·95	–	–	2·4	77·8	19·9
S83-05	S83__GZ11	groundmass	57·89	b.d.l.	25·36	–	0·44	b.d.l.	b.d.l.	8·13	5·10	3·58	n.a.	b.d.l.	100·50	–	–	37·6	42·7	19·7
S92-05	S92__GZ32	core (micro-phenocryst)	50·82	b.d.l.	30·75	–	0·60	b.d.l.	b.d.l.	14·12	3·73	0·29	n.a.	b.d.l.	100·30	–	–	66·5	31·8	1·6
Spinels																				
S7-05	S7__31	groundmass	1·90	22·16	5·60	14·28	49·67	0·64	3·22	n.a.	n.a.	n.a.	2·72	b.d.l.	100·19	10·4	24·6	–	–	–
S68-05	S68__GZ19	groundmass	0·13	18·84	3·26	26·67	44·71	0·60	2·75	n.a.	n.a.	n.a.	3·70	b.d.l.	100·67	9·9	43·2	–	–	–
S91-05	S91__GZ22	inclusion in ol	0·22	0·58	42·95	6·96	18·39	0·19	13·55	n.a.	n.a.	n.a.	16·76	0·16	99·77	56·8	20·7	–	–	–
S103-05	S103__GZ11	inclusion in ol phenocryst	0·13	11·84	9·19	21·90	33·71	0·31	6·68	n.a.	n.a.	n.a.	16·98	b.d.l.	100·73	26·1	55·3	–	–	–
Amphibole																				
S72-05a†		megacryst ($n=7$)	40·69	5·13	14·43	–	10·93	0·13	12·26	9·92	3·00	1·93	–	–	100·49‡	66·7	–	–	–	–

*Fe_2O_3 in spinels calculated assuming perfect stoichiometry.
†Geochemistry of the host rock is not available.
‡Includes 2·06 wt % H_2O (calculated).
Mg-number = mol % $Mg/(Mg+Fe^{2+})$; Cr-number = mol % $Cr/(Cr+Al)$; b.d.l., below detection limit; n.a., not analysed; –, not calculated.

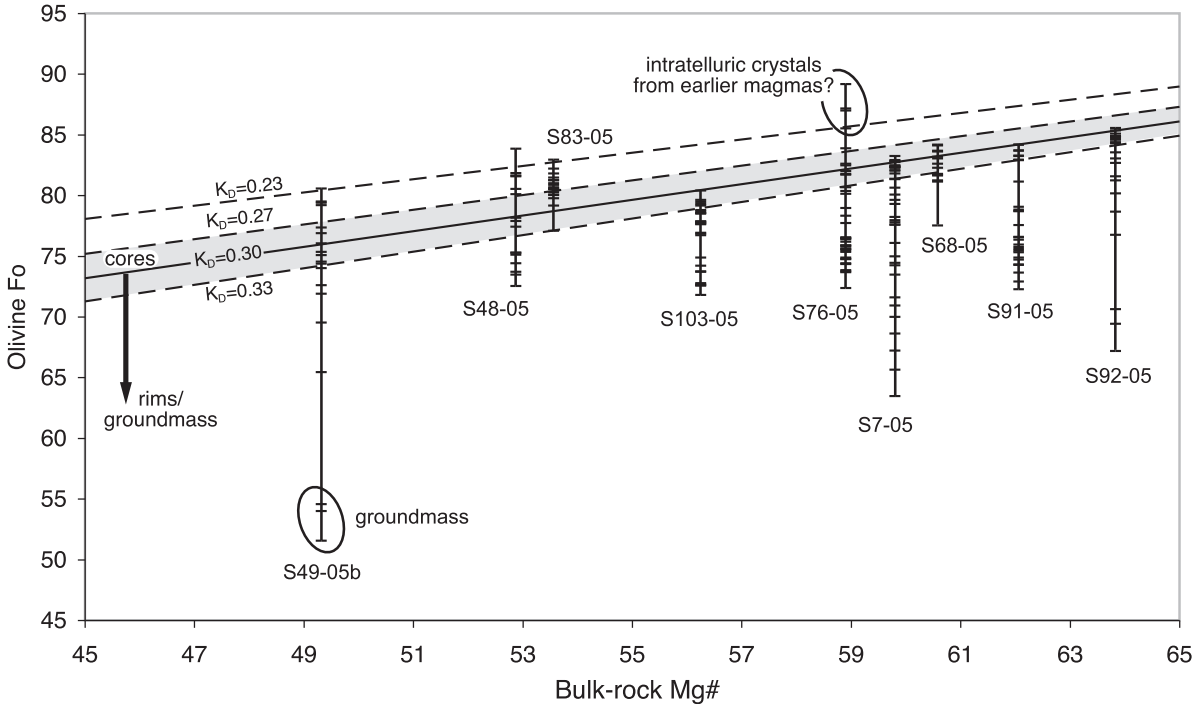

Fig. 3. Olivine forsterite (Fo) content (mol % Fo) vs bulk-rock Mg-number [mol % $Mg/(Mg + Fe^{2+})$, assuming 10% total iron oxide is ferric]. Sub-horizontal lines show predicted olivine Fo contents in equilibrium with the bulk-rock, using different values of the Fe–Mg partition coefficient (K_D). The grey field marks the range of K_D from Roeder & Emslie (1970). Vertical lines connect analyses (shown by small bars) from the same samples.

Plagioclase phenocrysts are labradorite ($An_{57–67}$), whereas plagioclases in the groundmass extend to lower anorthite components ($An_{38–68}$). Rare, rounded anorthoclase megacrysts ($An_{2–3}Or_{19–21}$), up to 3·5 mm in size, are observed in lavas from northern Al Ghab.

BULK-ROCK GEOCHEMISTRY

Degree of alteration

Most of the analysed samples are petrographically fresh and show little or no alteration. Iddingsite is present in some samples and several of these also show sericite replacement of plagioclase; these samples were not used for geochemical analysis. Loss on ignition (LOI) values range from −0·3 to 3·4 wt % (mostly <2 wt %). The small gain in mass after ignition seen in a few samples presumably results from oxidation of Fe^{2+} to Fe^{3+}. No correlation exists between LOI and the amounts of CaO and incompatible mobile elements such as K, Na, Rb and U, suggesting that the effects of alteration are negligible. In the following discussion, all the major oxides used in diagrams and reported in the text are normalized to an anhydrous basis with total iron recast as FeO_T.

Major and trace element variations

Figure 4 shows a series of major and trace element vs MgO variation diagrams for samples from the present study, along with appropriate crystal fractionation vectors. The ranges of MgO are similar for both volcanic groups (Homs 5·8–11·7 wt %; Al Ghab 5·8–10·4 wt %) and the MgO contents correlate negatively with Al_2O_3 and SiO_2, and positively with CaO/Al_2O_3, Ni and Cr. Compared with the Homs volcanic rocks at the same MgO, the Al Ghab volcanic rocks tend to exhibit lower SiO_2 and Al_2O_3, and higher TiO_2, Na_2O, K_2O, P_2O_5, large ion lithophile elements (LILE) and high field strength elements (HFSE).

On primitive-mantle normalized multi-element variation diagrams (Fig. 5a and b), the two volcanic groups display similar patterns but different degrees of incompatible element enrichment owing to the dominance of basanites in the younger series (Al Ghab group). Overall, the N-DSFS volcanic rocks have strong enrichment of most of the incompatible elements relative to primitive mantle and concave-upward patterns that peak at Nb, similar to many OIB (Sun & McDonough, 1989). These enrichments are coupled with relative depletions of K, Pb, Zr and Rb and relative enrichments of Ba, Sr–P and Ti. The size of

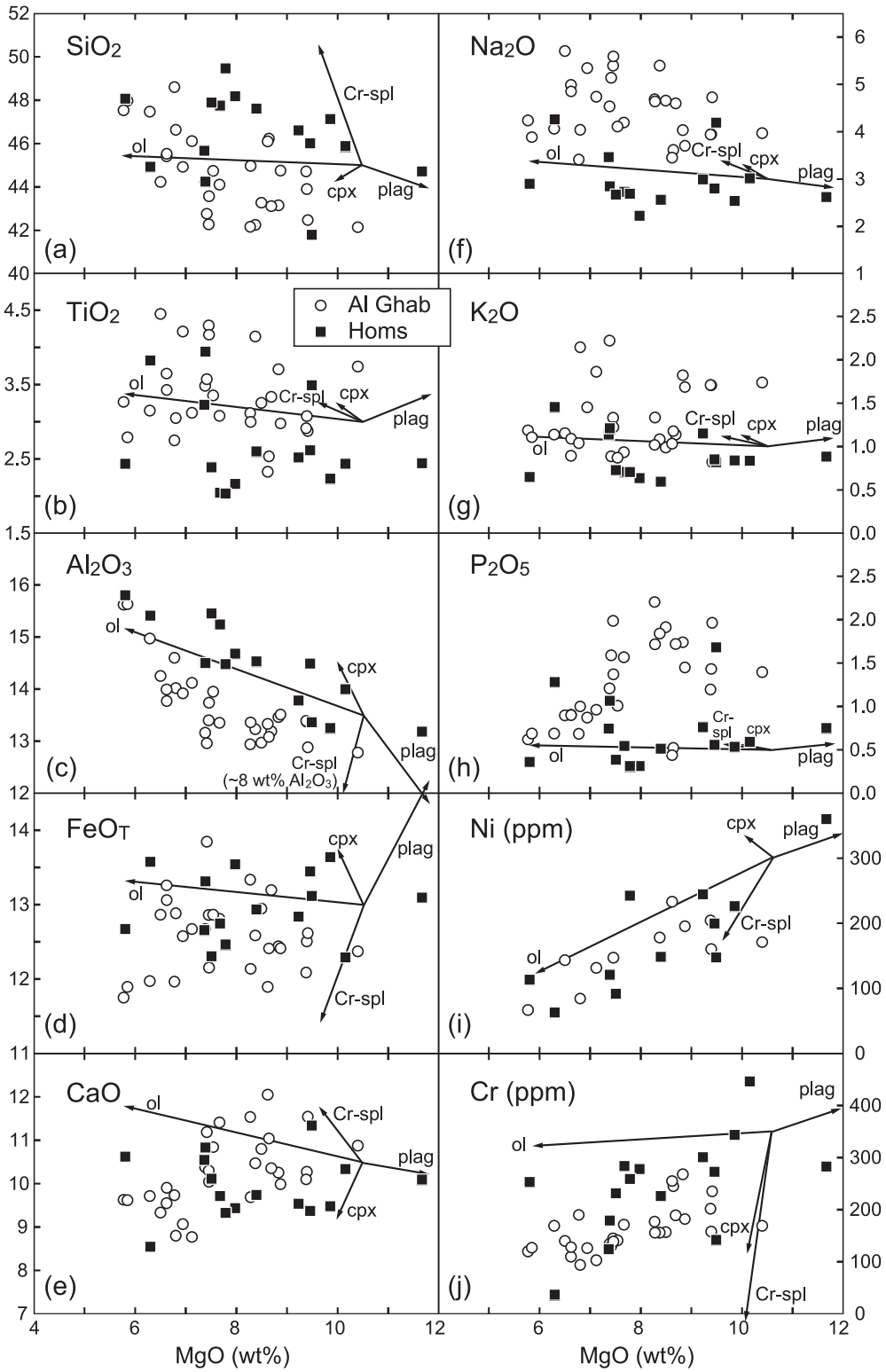

Fig. 4. Major elements (wt %) and selected trace elements (ppm) vs MgO (wt %) for samples from this study. Arrows are fractionation vectors showing approximately 10% fractionation of each mineral from a hypothetical liquid composition.

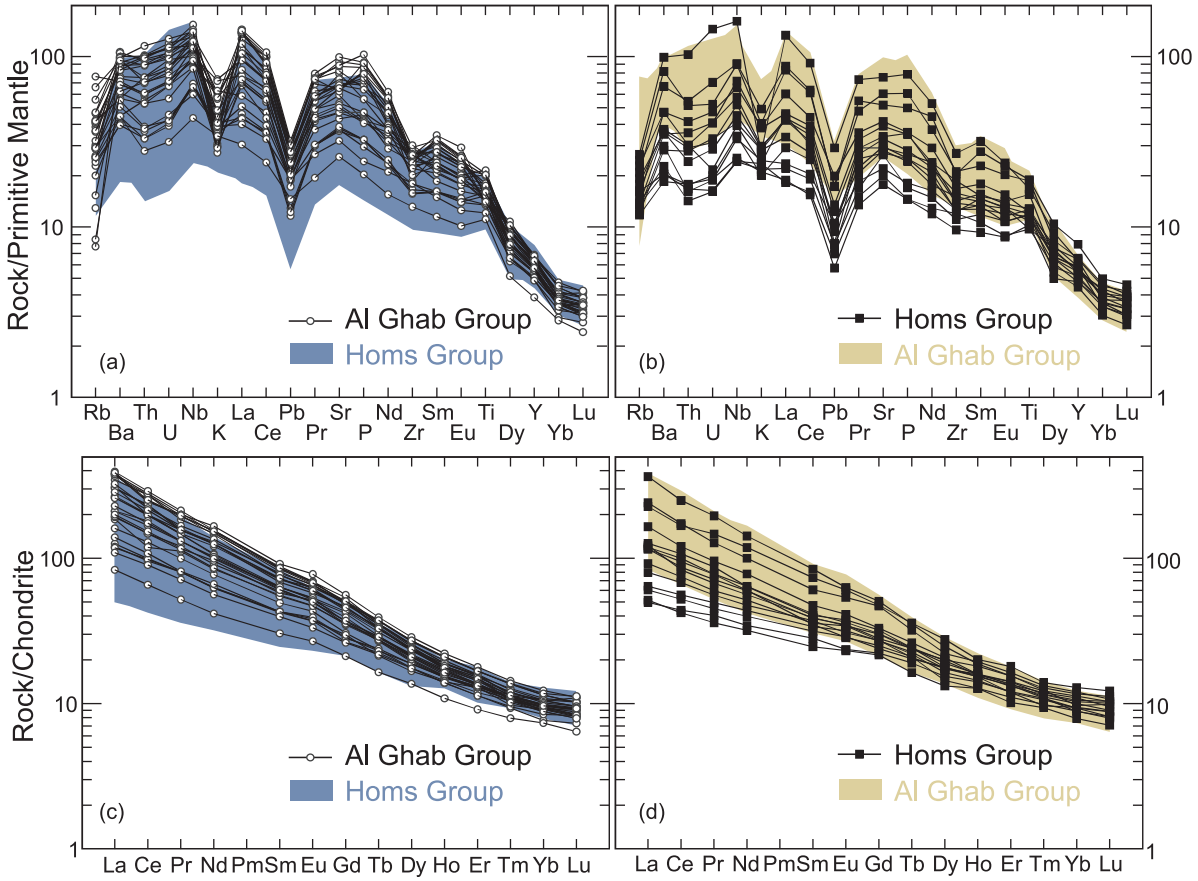

Fig. 5. Primitive-mantle and chondrite normalized multi-element variation diagrams for the Homs and Al Ghab volcanic groups. Shaded fields in (a) and (c) indicate the compositional range of the Homs volcanic group and in (b) and (d) the Al Ghab volcanic group. Primitive mantle and chondrite normalizing values are from McDonough & Sun (1995) and Sun & McDonough (1989), respectively.

most of these anomalies (e.g. K, Zr and Rb) is related to the ratio of very incompatible elements to moderately incompatible elements (e.g. La/Yb), as well as to the SiO_2 content. This point will be considered further when discussing the genesis of the magmas.

On chondrite-normalized rare earth element (REE) diagrams (Fig. 5c and d), the REE are variably fractionated with La ranging from ~40 to ~300 times chondrite. The Al Ghab volcanic rocks show a wide range of $(La/Yb)_N$ between 11·3 and 40·1, whereas the majority of the Homs volcanic rocks show a narrower and lower range of $(La/Yb)_N$ between 5·4 and 16·5 with few basanites up to 37·5. No significant Eu-anomaly [$Eu/Eu^* = 0{\cdot}95–1{\cdot}18$; $Eu/Eu^* = Eu_N/\sqrt{(Sm_N \times Gd_N)}$] has been observed in any of the samples.

Nd–Sr–Pb isotopic compositions

Nine representative Al Ghab–Homs basalts were analysed in this study for Nd and Sr isotopes, and five for Pb isotopes (Table 3). The basalts are young, therefore no age correction has been made for the isotopic ratios. Selected literature data for volcanic rocks (Abdel-Rahman & Nassar, 2004; Lustrino & Sharkov, 2006; Krienitz *et al.*, 2009) from the same study area are also included in the following descriptions and Fig. 6 to augment the new data (Appendix B). In general, both volcanic groups exhibit limited and similar ranges of Sr, Nd and Pb isotopic compositions [Homs: $^{87}Sr/^{86}Sr = 0{\cdot}70306–0{\cdot}70348$, $^{143}Nd/^{144}Nd = 0{\cdot}51284–0{\cdot}51295$ ($\varepsilon Nd = +4{\cdot}0$ to $+6{\cdot}1$), $^{206}Pb/^{204}Pb = 18{\cdot}72–19{\cdot}59$, $^{207}Pb/^{204}Pb = 15{\cdot}56–15{\cdot}65$, $^{208}Pb/^{204}Pb = 38{\cdot}52–39{\cdot}34$; Al Ghab: $^{87}Sr/^{86}Sr = 0{\cdot}70316–0{\cdot}70359$, $^{143}Nd/^{144}Nd = 0{\cdot}51290–0{\cdot}51299$ ($\varepsilon Nd = +5{\cdot}1$ to $+6{\cdot}9$), $^{206}Pb/^{204}Pb = 18{\cdot}82–19{\cdot}32$, $^{207}Pb/^{204}Pb = 15{\cdot}55–15{\cdot}62$, $^{208}Pb/^{204}Pb = 38{\cdot}69–39{\cdot}10$], and overlap the ranges of PREMA (Prevalent Mantle) and LVC (Low Velocity Component) (Fig. 6a; Wörner *et al.*, 1986; Hoernle *et al.*, 1995).

In Fig. 6b, the basalts display a negative correlation between $^{87}Sr/^{86}Sr$ and $^{143}Nd/^{144}Nd$, although one sample (SY-101 of Krienitz *et al.*, 2009) lies above the main array. Their compositions are similar to those of the intraplate volcanic rocks of southern Syria, Jordan and Israel, which

Table 3: Sr, Nd and Pb isotopic data for selected N-DSFS lavas analysed in this study

Sample	$^{87}Sr/^{86}Sr$ (±2σ)	$^{143}Nd/^{144}Nd$ (±2σ)	εNd	$^{206}Pb/^{204}Pb$ (±2σ)	$^{207}Pb/^{204}Pb$(±2σ)	$^{208}Pb/^{204}Pb$ (±2σ)	Δ7/4	Δ8/4
S7-05	0·70319 (1)	0·512911 (5)	5·33	19·320 (25)	15·622 (19)	39·100 (52)	3·72	11·46
S10-05	0·70322 (2)	0·512909 (5)	5·29					
S59-05	0·70352 (1)	0·512898 (6)	5·07	18·815 (21)	15·551 (16)	38·690 (44)	2·09	31·60
S68-05	0·70319 (1)	0·512916 (6)	5·42					
S76-05	0·70326 (2)	0·512898 (7)	5·06	19·586 (22)	15·648 (16)	39·324 (44)	3·43	3·58
S92-05	0·70313 (1)	0·512924 (6)	5·59	18·830 (20)	15·565 (16)	38·705 (42)	3·33	31·29
S101-05	0·70335 (1)	0·512912 (7)	5·34	18·981 (22)	15·582 (16)	38·748 (44)	3·39	17·24
S103-05	0·70348 (1)	0·512841 (7)	3·96					
S105-05	0·70336 (2)	0·512850 (7)	4·14					

εNd was calculated using modern $(^{143}Nd/^{144}Nd)_{CHUR} = 0·512638$ (Goldstein *et al.*, 1984). Δ7/4 and Δ8/4 were calculated according to Hart (1984).

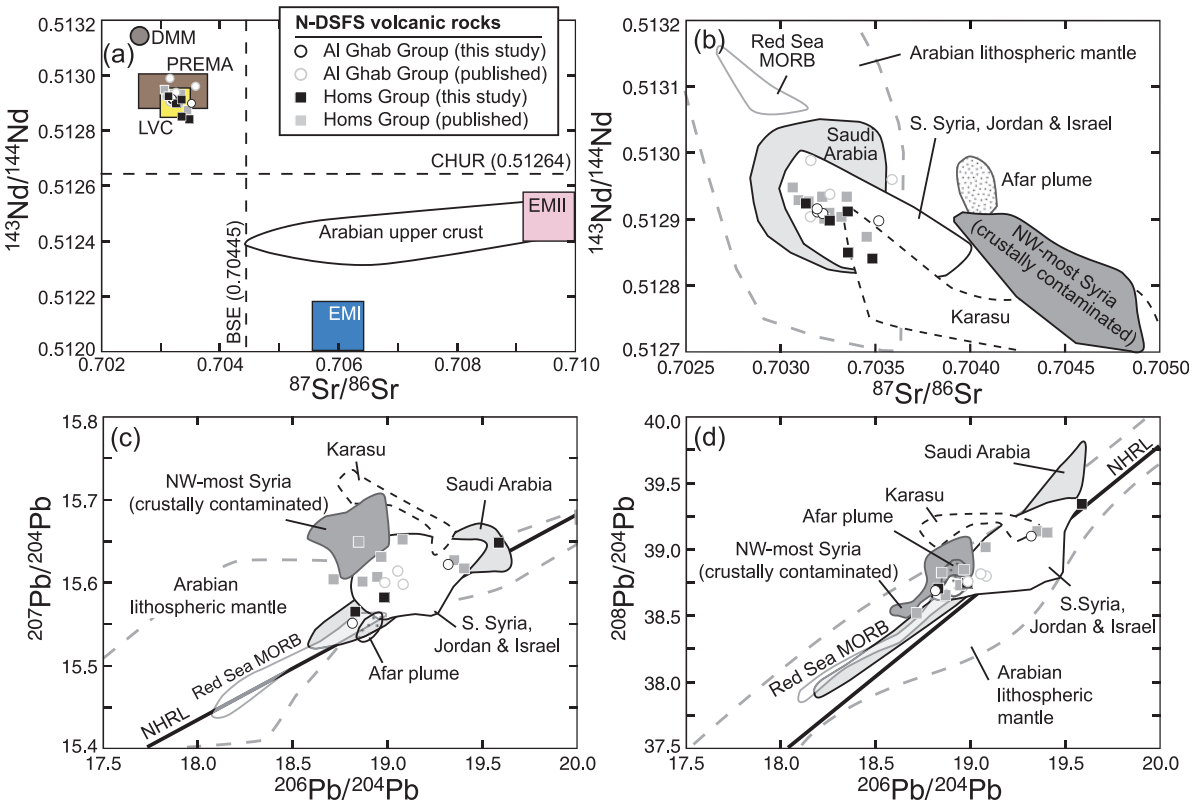

Fig. 6. (a, b) $^{87}Sr/^{86}Sr$ vs $^{143}Nd/^{144}Nd$, (c) $^{207}Pb/^{204}Pb$ vs $^{206}Pb/^{204}Pb$ and (d) $^{208}Pb/^{204}Pb$ vs $^{206}Pb/^{204}Pb$ for the N-DSFS lavas analysed in this study and elsewhere. Plotted for comparison are Cenozoic intraplate volcanic rocks from northwesternmost Syria (Krienitz *et al.*, 2006), Karasu (Çapan *et al.*, 1987), and Saudi Arabia (discarding two samples with very high Δ7/4), southern Syria, Jordan and Israel (Altherr *et al.*, 1990; Stein & Hofmann, 1992; Bertrand *et al.*, 2003; Shaw *et al.*, 2003; Weinstein *et al.*, 2006; Krienitz *et al.*, 2007). Additional fields shown for comparison include the Arabian lithospheric mantle (cpx separates from mantle xenoliths; Henjes-Kunst *et al.*, 1990; Stein *et al.*, 1993; Blusztajn *et al.*, 1995; Baker *et al.*, 1998, 2002; Shaw *et al.*, 2007; Nasir & Rollinson, 2009), Red Sea MORB mantle (Volker *et al.*, 1993), the high $^{3}He/^{4}He$ Afar plume (Pik *et al.*, 1999), Arabian upper continental crust (Hegner & Pallister, 1989; Jarrar *et al.*, 2003), Depleted MORB Mantle (DMM) (Workman & Hart, 2005), Enriched Mantle I (EMI) (Lustrino & Dallai, 2003), Enriched Mantle II (EMII) (Workman *et al.*, 2004), Low Velocity Component (LVC) (Hoernle *et al.*, 1995) and Prevalent Mantle (PREMA) (Wörner *et al.*, 1986). In (a), the Bulk Silicate Earth estimate (BSE) and Chondritic Uniform Reservoir (CHUR) are from DePaolo (1988) and Goldstein *et al.* (1984), respectively. In (c) and (d), the Northern Hemisphere Reference Line (NHRL) is from Hart (1984).

extend to somewhat more radiogenic $^{87}Sr/^{86}Sr$ compositions. Saudi Arabian samples are characterized by a larger range, extending to higher Nd and lower Sr isotopic values. The volcanic fields of northwesternmost Syria and the Karasu Valley, southern Turkey, are geographically close to the present study area, but are compositionally distinct in that they have significantly higher Sr and lower Nd isotopic values. Some potential mantle source compositions including the Afar plume, Red Sea mid-ocean ridge basalt (MORB) mantle and Arabian lithospheric mantle are also shown in Fig. 6. Compared with the N-DSFS basalts, the Red Sea MORB mantle has a more radiogenic $^{143}Nd/^{144}Nd$ and less radiogenic $^{87}Sr/^{86}Sr$ composition, whereas the Afar plume has a more radiogenic $^{87}Sr/^{86}Sr$ composition. The Arabian lithospheric mantle encompasses all the N-DSFS basalts, but has a very wide range of isotopic compositions.

The Pb–Pb isotopic variations are shown in Fig. 6c and d. Samples from the N-DSFS define a positive correlation in $^{206}Pb/^{204}Pb$–$^{207}Pb/^{204}Pb$ and $^{206}Pb/^{204}Pb$–$^{208}Pb/^{204}Pb$ space, although the correlation is weaker for $^{206}Pb/^{204}Pb$ vs $^{207}Pb/^{204}Pb$. All the samples fall above the Northern Hemisphere Reference Line (NHRL) as established by Hart (1984). There does not appear to be any clear Sr–Pb and Nd–Pb isotopic correlation. The compositions of basalts from the N-DSFS overlap with those from Saudi Arabia, southern Syria, Jordan and Israel, and are clearly distinct (higher $^{207}Pb/^{204}Pb$ and $^{208}Pb/^{204}Pb$) from Red Sea MORB samples. The volcanic rocks of northwesternmost Syria and Karasu are offset to higher $^{207}Pb/^{204}Pb$ and $^{208}Pb/^{204}Pb$ relative to the N-DSFS basalts, probably as a result of crustal contamination (Çapan *et al.*, 1987; Krienitz *et al.*, 2006), whereas the Afar plume is distinct in having relatively low $^{207}Pb/^{204}Pb$ ratios. Similar to the observation in Sr–Nd space, the Arabian lithospheric mantle has a wide Pb isotopic compositional range and encompasses nearly all the N-DSFS basalt compositions.

DISCUSSION

Effect of low-pressure fractional crystallization

The N-DSFS lavas display a range of MgO contents with associated variations in Ni and Cr (Fig. 4). This, together with the presence of abundant olivine and some clinopyroxene phenocrysts in the lavas, is suggestive of crystal fractionation during magma ascent. In both volcanic groups, the dominant fractionation assemblage appears to be olivine ± clinopyroxene ± spinel as indicated by the increasing SiO_2 and Al_2O_3, and decreasing Ni and Cr with decreasing MgO. Some scatter in FeO_T and CaO vs MgO may reflect varying extents of clinopyroxene and/or spinel fractionation or accumulation, in accord with our observation that clinopyroxene phenocrysts do not occur in all samples and several samples (e.g. S48-05) with low Mg-number have accumulated up to ~10% clinopyroxene phenocrysts. There is little evidence for plagioclase fractionation, as Eu anomalies are lacking, and Al_2O_3 does not show a decrease with decreasing MgO.

As described above, the Homs and Al Ghab volcanic groups show essentially sub-parallel trends for MgO vs SiO_2 and Al_2O_3, coupled with wide and different ranges of incompatible element abundances [e.g. P_2O_5, K_2O, Na_2O, TiO_2, LILE, HFSE and light REE (LREE)]. These variations are not readily explained by simple low-pressure crystal fractionation alone and must reflect source heterogeneity or varying degrees of partial melting.

Crustal contamination vs source heterogeneity

Upon segregation from their mantle source region, the magmas may have stagnated at various levels within the continental lithosphere during their ascent to the surface, fractionally crystallizing and assimilating crustal materials, which thereby altered the compositions of the primitive magmas. One common way to assess the significance of crustal contamination is to look at the variation in the Nd and Sr isotopic compositions of the basalts, recognizing that continental crust has high $^{87}Sr/^{86}Sr$ and low $^{143}Nd/^{144}Nd$ values. To explore this process, various possible candidates for assimilation are considered. The isotopic composition and even the nature of the basement beneath Syria is poorly known at present. Of the limited available published data, crust similar to the Jordanian Late Proterozoic Arabian Shield (Jarrar *et al.*, 2003), which as a prerequisite possesses radiogenic $^{87}Sr/^{86}Sr$ and unradiogenic $^{143}Nd/^{144}Nd$, is a more viable assimilant than the geographically more distal and isotopically more extreme Early Proterozoic–Late Archean crust of Yemen, Sudan and Tanzania. Assimilation–fractional crystallization (AFC) calculations were performed using a typical upper crustal composition from southern Jordan and a lower crustal composition from southern Syria (Table 4) as the contaminants; the results are illustrated in Fig. 7.

In the upper-crust contamination model (Fig. 7a), the AFC curves pass through only the 'upper array', and the most contaminated samples are SY-174 (sample of Krienitz *et al.*, 2009) and S59-05 with a maximum of ~6% assimilation of a Late Proterozoic upper crustal component. These two samples also exhibit $Ce/Pb \leq 18$, amongst the lowest of all the samples, a situation expected for contamination by continental crust [e.g. bulk continental crust reported by Taylor & McLennan (1995) has $Ce/Pb = 4{\cdot}1$]. Other than these, the majority of the samples have lower $^{143}Nd/^{144}Nd$ than the two model AFC curves at similar $^{87}Sr/^{86}Sr$, suggesting that other crustal components or source heterogeneity have to be invoked.

The lower-crust contamination curves (Fig. 7b) with variable D_{Sr} can better account for the Nd–Sr isotopic

Table 4: Parameters used in the AFC modelling

	Assimilant composition		Starting magma composition		
	UC*	LC†	SY-157‡	Low 6/4 component§	High 6/4 component§
$^{87}Sr/^{86}Sr$	0·7064	0·70423	0·70306	0·70309	0·70325
Sr (ppm)	650	582	1146	800	1500
$^{143}Nd/^{144}Nd$	0·5124	0·51274	0·51295		
Nd (ppm)	22·5	25·3	38·8		
$^{206}Pb/^{204}Pb$	18·5			18·7	19·6
Pb (ppm)	12·5			2	4·5

	Partition coefficient¶
D_{Sr}	0·2–2
D_{Nd}	0·2
D_{Pb}	0·2

*Late Proterozoic upper crustal composition: $^{87}Sr/^{86}Sr$, $^{143}Nd/^{144}Nd$, and Sr and Nd abundances are the weighted average of basement rocks from Jordan (Jarrar *et al.*, 2003), excluding three samples with extremely high $^{87}Sr/^{86}Sr$ (>0·713); $^{206}Pb/^{204}Pb$ and Pb abundance are the weighted average of basement rocks from Saudi Arabia (Hegner & Pallister, 1989).
†Lower crustal compositional average of three xenoliths from southern Syria (Krienitz, 2004).
‡Composition of basanite SY-157 from Homs volcanic field (Krienitz *et al.*, 2009).
§Isotopic end-member compositions of the low 6/4 component and the high 6/4 component are as in Table 5, whereas the Sr and Pb abundances are approximated to the average of several lava samples whose isotopic compositions approach the corresponding end-member components.
¶Values assumed.

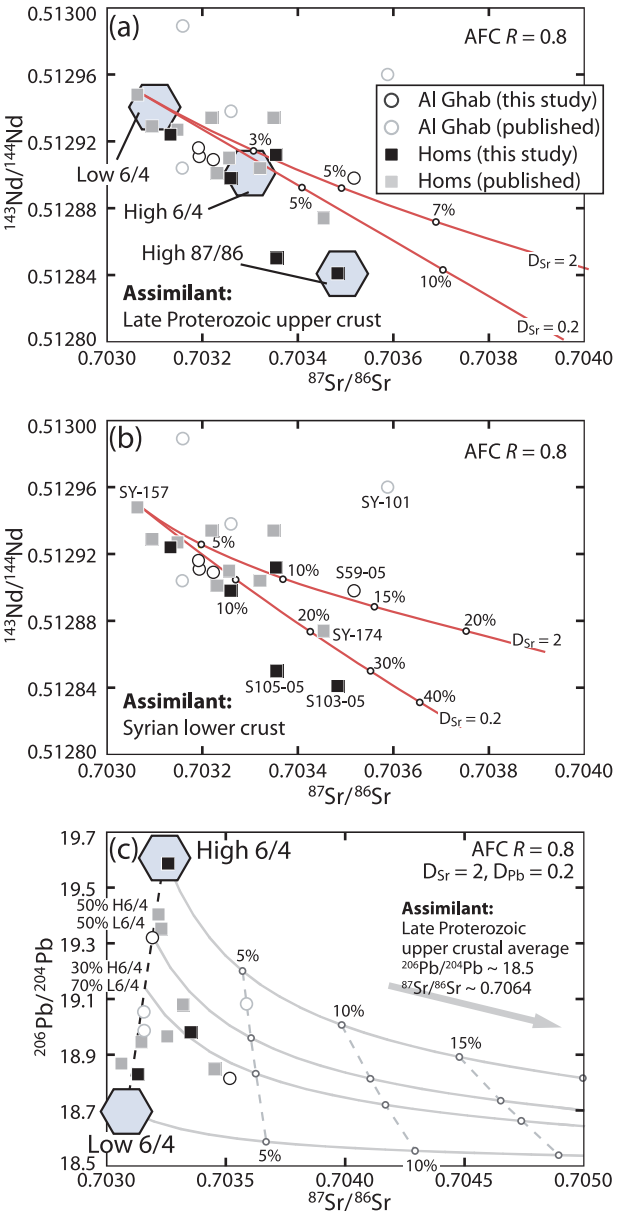

Fig. 7. Forward AFC modelling (DePaolo, 1981) on the basis of (a, b) $^{143}Nd/^{144}Nd$ vs $^{87}Sr/^{86}Sr$ and (c) $^{206}Pb/^{204}Pb$ vs $^{87}Sr/^{86}Sr$ for the N-DSFS lavas. The initial magma composition is assumed to be that of SY-157 (Krienitz *et al.*, 2009) in (a) and (b). Also shown in (a) are three inferred mantle end-member components (shaded hexagons), the low 6/4 component, high 6/4 component and high 87/86 component as discussed in the text and listed in Table 5. The percentages along the grey model curves indicate the amounts of AFC. *R*, ratio of rate of assimilation to rate of crystallization, is assumed to be 0·8 in all models. The composition of assimilants and other parameters are listed in Table 4. In (c), most of the compositional variability of the lavas can be explained by variable amounts of bulk-mixing between the low 6/4 component and the high 6/4 component (black dashed line), which are considered to represent mantle heterogeneities. Several samples with higher $^{87}Sr/^{86}Sr$ can be explained by assimilation (≤5%) of Late Proterozoic upper crust. H6/4, high 6/4 component; L6/4, low 6/4 component.

variations of the N-DSFS lavas. However, the required amounts of AFC are very large (up to ~22%, or even ~30% if Sl03-05 is also considered) and are considered thermodynamically not feasible. Moreover, there are still many samples (e.g. Sl03-05 and Sl05-05) that plot below these curves, suggesting source heterogeneity.

On a plot of $^{87}Sr/^{86}Sr$ vs $^{206}Pb/^{204}Pb$ (Fig. 7c), some insight can be gained into the relative role of source heterogeneity and crustal contamination. There are considerable $^{206}Pb/^{204}Pb$ variations at low $^{87}Sr/^{86}Sr$ values in the N-DSFS samples. These low $^{87}Sr/^{86}Sr$ samples are coupled with high $^{143}Nd/^{144}Nd$ (Fig. 7a), indicative of a primitive isotopic signature inherited from a somewhat depleted mantle source. The varying $^{206}Pb/^{204}Pb$ at relatively constant, low, $^{87}Sr/^{86}Sr$ values is inconsistent with a

contribution from either a locally available upper or lower continental crustal component, which should elevate the $^{87}Sr/^{86}Sr$ content of the basalts (Fig. 7a and b). It is therefore considered that the variable $^{206}Pb/^{204}Pb$ compositions are intrinsic to the source(s). The corresponding low and high $^{206}Pb/^{204}Pb$ end-members are hereby assigned as the 'low 6/4 component' and the 'high 6/4 component', respectively, in the following discussion. There are a few samples characterized by $^{87}Sr/^{86}Sr$ more radiogenic than the assumed low 6/4 component and high 6/4 component. These have also been influenced by crustal contamination. Specifically, AFC modelling suggests ≤5% assimilation of Late Proterozoic upper crust by magmas with varying portions of the low 6/4 and high 6/4 components (Fig. 7c).

Although a crustal contaminant has been identified based on the isotopic compositions of some of the lavas, several lines of evidence argue against a major role for contamination in the petrogenesis of the N-DSFS basalts as a whole. First, many of the Al Ghab volcanic rocks contain mantle-derived xenoliths, suggesting rapid lava ascent to the surface, thus avoiding considerable assimilation of crustal materials. Second, the amounts of AFC modelled above are generally low, less than ~6% (the upper crust model; Fig. 7a). Third, most of the N-DSFS basalts have Ce/Pb, Nb/U, K/Nb and Th/Nb similar to OIB (Fig. 8; GEOROC data compilation). There are only few data points with reduced Ce/Pb and elevated Ba/Nb, displaced towards the composition of the continental crust (Fig. 8). This, together with a lack of Ce/Pb–$^{87}Sr/^{86}Sr$ (and $^{143}Nd/^{144}Nd$) correlations amongst the N-DSFS data, further supports the interpretation that crustal contamination affected only a small subset of samples.

To summarize, the main isotopic variations appear to be a result of source heterogeneity. Two components with similarly low $^{87}Sr/^{86}Sr$ and varying $^{206}Pb/^{207}Pb$ have been identified (Table 5). Because these two components are characterized by unradiogenic $^{87}Sr/^{86}Sr$, there must be a third component, with high $^{87}Sr/^{86}Sr$ and low $^{143}Nd/^{144}Nd$, to account for the continuous Nd–Sr isotopic array. This component, hereby assigned as the high 87/86 component, is best exemplified by S103-05 and S105-05, which have high Ce/Pb and low Ba/Nb, typical of uncontaminated basalts. Their low LOI as well as their petrographic characteristics preclude the radiogenic Sr isotope signature being the result of alteration. Unfortunately, the Pb isotope composition of the high 87/86 component is unclear, as insufficient data are available. In subsequent discussions of source characteristics, only samples with Ce/Pb ≥ 21 and Ba/Nb ≤ 10 are considered, to avoid crustally contaminated samples.

Comparison of the N-DSFS magmas with partial melting experimental data

Numerous partial melting experiments provide constraints on basalt genesis. A comparison of the N-DSFS lavas with these isobaric experimental melts may be insightful, before any petrogenetic modelling is performed. Following Thompson *et al.* (2005), the least evolved N-DSFS lavas (≥8 wt % MgO and crustally uncontaminated) are plotted on the CIPW normative Di–Ol–Hy–(Ne + Lc)–Qz projection along with some of the representative experimental mantle melts (Fig. 9).

The compositions of partial melts of anhydrous and carbonated fertile lherzolite (KLB-1 and similar compositions) from a range of experimental studies (Hirose & Kushiro, 1993; Takahashi *et al.*, 1993; Kushiro, 1996; Falloon *et al.*, 1997, 1999; Hirose, 1997; Hirschmann *et al.*, 1998; Robinson *et al.*, 1998; Walter, 1998; Dasgupta *et al.*, 2007) are summarized and highlighted as progressive melting trends (from ~3% to ~40–45%; arrows in Fig. 9). These trends occupy much of the space on the Di–Ol–Hy plane, whereas nearly all the N-DSFS lavas plot on the nepheline-normative plane, with samples of the Al Ghab group generally having higher normative nepheline than those of the Homs group. The N-DSFS samples, particularly those of the Al Ghab group, are similar to the anhydrous partial melts generated by progressive melting at 1 and 1·5 GPa. The Homs samples fall between the two melting trends for carbonated peridotite; however, in the experiments of Dasgupta *et al.* (2007) such partial melts are composed of 4–25 wt % dissolved CO_2 and tend to be very Ca-rich and Si-, Ti- and alkali (especially K)-poor, characteristics that are not observed for the Homs magmas.

There has long been concern that anhydrous fertile lherzolite cannot alone be the source of OIB-like (especially Ne-normative) magmas, regardless of how closely similar the CIPW norms are between the N-DSFS lavas and experimental peridotite melts. One important argument is that OIB magmas are too enriched in Fe and Ti, but too depleted in Si and Al, which may be better explained by incorporation of an additional mafic component in the source (e.g. Prytulak & Elliott, 2007, and references therein). Lithologies such as pyroxenite, hornblendite and melts thereof have been considered the source of this 'mafic component' in OIB (Hirschmann *et al.*, 2003; Kogiso *et al.*, 2003, 2004; Pilet *et al.*, 2008; Humphreys & Niu, 2009; Niu, 2009). It has been suggested that tholeiitic magmas might incorporate a component of partial melt from silica-excess pyroxenites (Kogiso *et al.*, 2004). However, such partial melts are generally Qz-normative and plot away from the Homs tholeiitic basalt (Ol–Hy normative) in Fig. 9.

Experimental partial melts of phlogopite-bearing metasomatized peridotite (2·8 GPa; Mengel & Green, 1989), silica-deficient garnet-pyroxenite (2–5 GPa; Hirschmann *et al.*, 2003; Kogiso *et al.*, 2003), hornblendite (1·5 GPa) and sandwiched hornblendite–depleted lherzolite (DMM-1; 1·5 GPa; Pilet *et al.*, 2008), however, have a clear and intimate relationship with the N-DSFS lavas on the

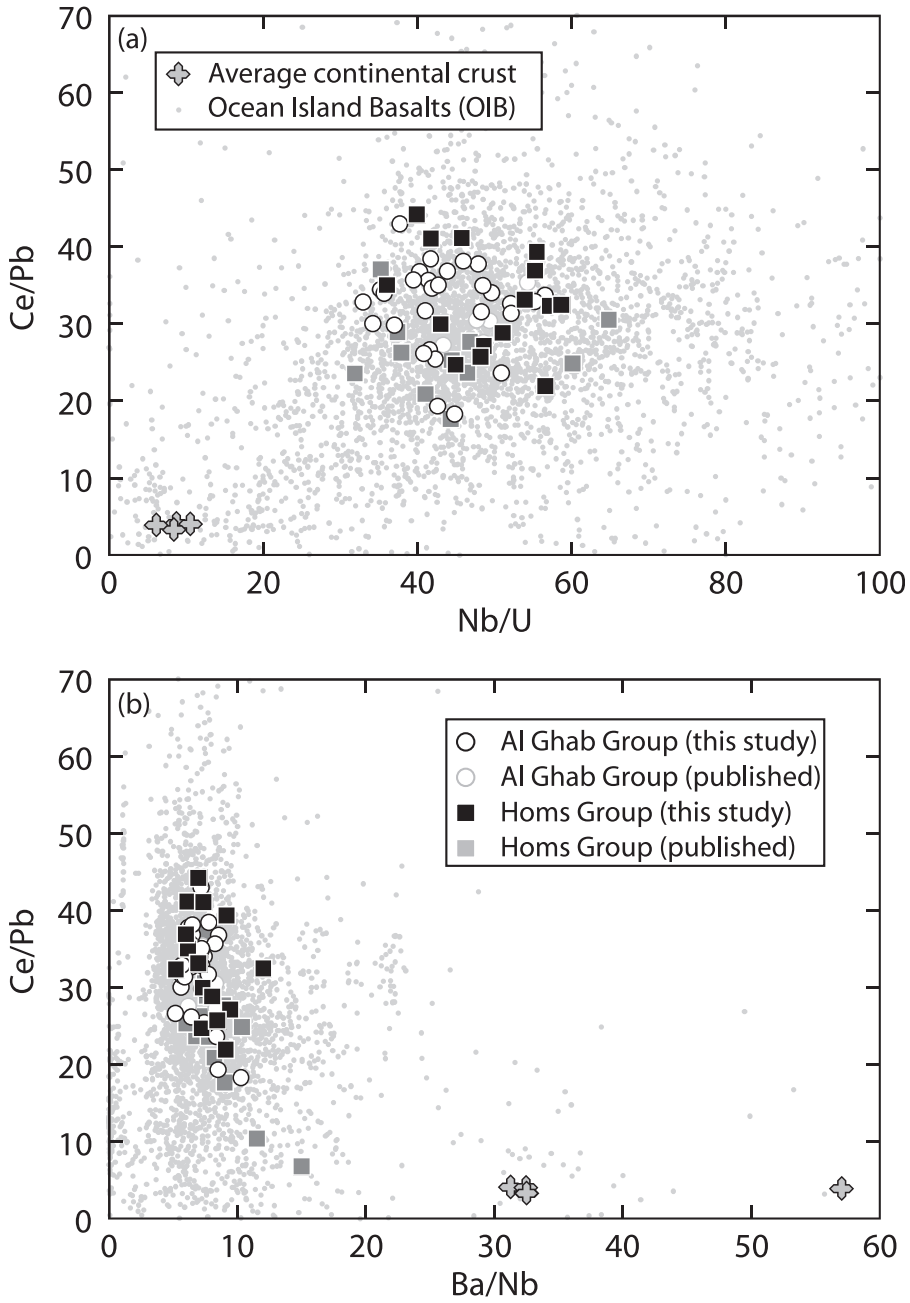

Fig. 8. (a) Ce/Pb vs Nb/U and (b) Ce/Pb vs Ba/Nb for N-DSFS basalts. Shown for comparison are the compositions of OIB (GEOROC database compilation) and average continental crust (Weaver & Tarney, 1984; Rudnick & Fountain, 1995; Taylor & McLennan, 1995; Wedepohl, 1995; Rudnick & Gao, 2003). In (b), some samples with low Ce/Pb are clearly displaced towards the average composition of the continental crust (high Ba/Nb), indicating that crustal assimilation may have affected them.

Di–Ol–(Ne + Lc) plane. In detail, the Al Ghab samples (mainly basanites) plot close to the hornblendite melts, whereas the Homs samples plot close to the sandwiched hornblendite–DMM-1 melts and within the compositional range of silica-deficient garnet-pyroxenite melts. It is noteworthy that the MgO contents of the silica-deficient garnet-pyroxenite melts (~11–15 wt %; Hirschmann *et al.*, 2003; Kogiso *et al.*, 2003) and particularly the various (both DMM-1 sandwiched and stand-alone) hornblendite melts (~7–13 wt %; Pilet *et al.*, 2008) are considerably lower than those of the experimental peridotite melts and comparable with those of the N-DSFS fractionation-uncorrected lavas. If these mafic lithologies do represent important components in the source of the N-DSFS

Table 5: Inferred isotopic compositions of mantle end-member components

Component*	$^{87}Sr/^{86}Sr$	$^{143}Nd/^{144}Nd$	$^{206}Pb/^{204}Pb$	Remark
Low 6/4 component	0·7031	0·51294	18·7	Wall-rock peridotite in the lithosphere that hosts the metasomatic veins
High 6/4 component	0·7033	0·51290	19·6	Metasomatic vein source within the lithosphere; the original isotopic compositions of the veins (probably somewhat heterogeneous) may be more 'extreme' as all the N-DSFS basanites now used for the identification of C_B have been influenced by the lithospheric peridotitic component, C_A (see also Fig. 10)
High 87/86 component	0·7035	0·51284	–	Independent sub-lithospheric (asthenospheric or plume?) source

–, no $^{206}Pb/^{204}Pb$ is available for samples that characterized the high 87/86 component. C_A is the low 6/4 component; C_B is the high 6/4 component.
*The nomenclature of the components was based on their diagnostic isotopic features, as exhibited by the crustally uncontaminated lavas.

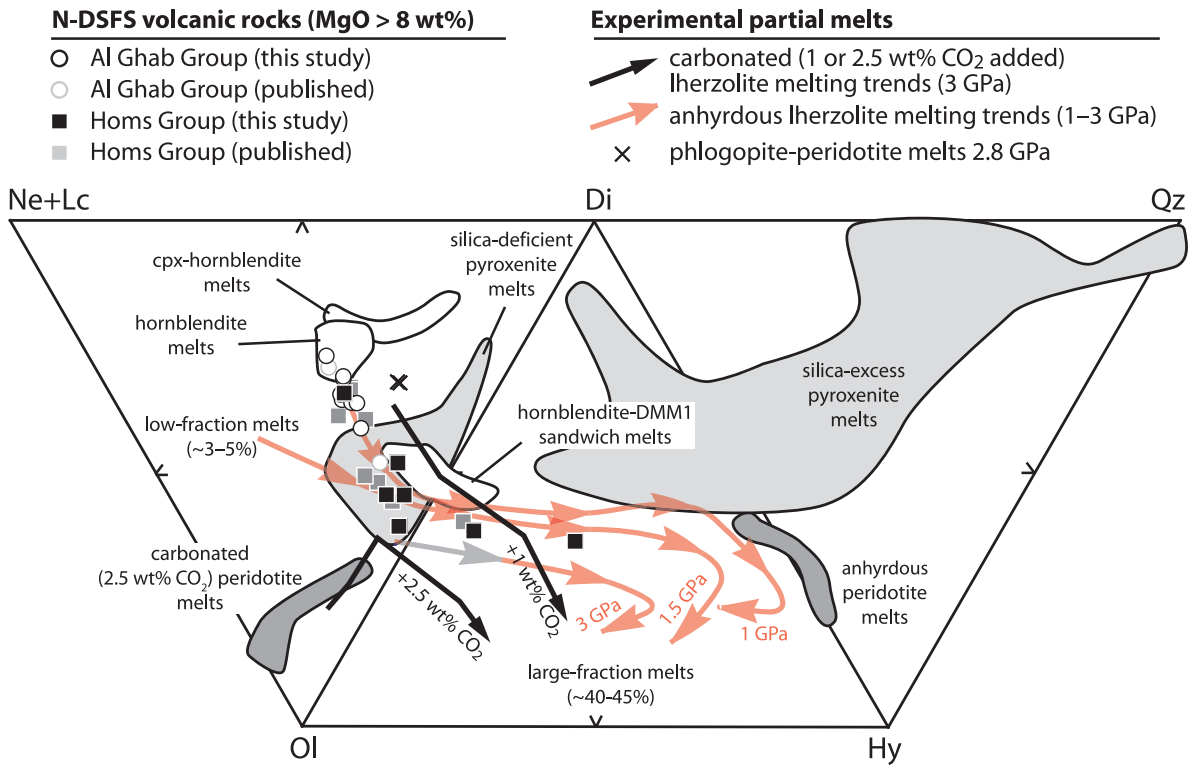

Fig. 9. CIPW normative diopside, olivine, hypersthene, nepheline + leucite and quartz variations in the relatively primitive, least crustally contaminated N-DSFS samples (MgO ≥ 8 wt %, Ce/Pb ≥ 21 and Ba/Nb ≤ 10). Also shown are the melt compositions in a range of partial melting experiments on various sources, including: phlogopite-bearing peridotite (Mengel & Green, 1989), carbonated peridotite (KLB-1) (Hirose, 1997; Dasgupta *et al.*, 2007), hydrous peridotite (KLB-1) (Hirose & Kawamoto, 1995), silica-deficient pyroxenite (MIX1G) (Hirschmann *et al.*, 2003; Kogiso *et al.*, 2003), silica-excess (G2 and JB-1) pyroxenite (Tsuruta & Takahashi, 1998; Pertermann & Hirschmann, 2003), hornblendite (AG4), clinopyroxene-hornblendite (AG7) and sandwiched hornblendite–depleted peridotite (DMM1) (Pilet *et al.*, 2008). Arrows show partial melting trends, at different pressures, for anhydrous peridotite (KLB-1 and similar compositions) based on the compilation of Thompson *et al.* (2005), and trends for CO_2-bearing peridotite (Dasgupta *et al.*, 2007). All data were calculated with 10% total iron as Fe_2O_3 (Thompson & Gibson, 2000).

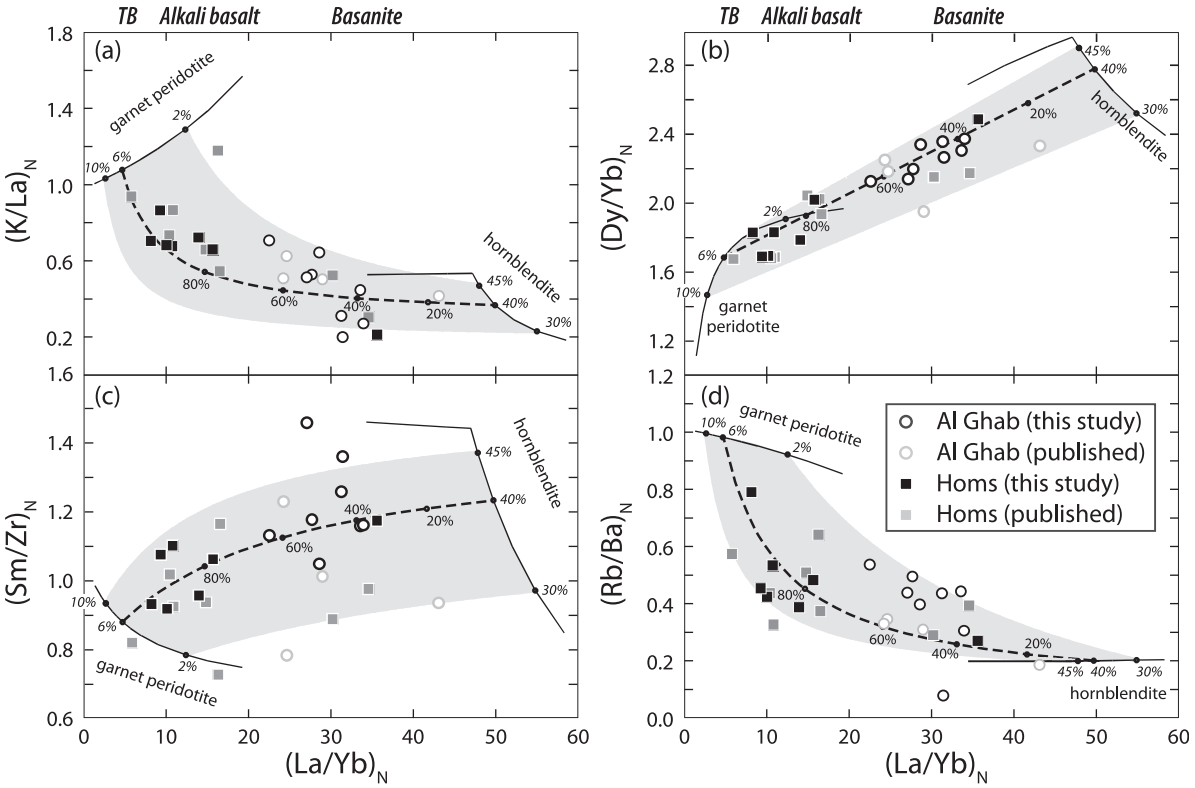

Fig. 10. (a) $(K/La)_N$, (b) $(Dy/Yb)_N$, (c) $(Sm/Zr)_N$ and (d) $(Rb/Ba)_N$ vs $(La/Yb)_N$ for the relatively primitive, least crustally contaminated N-DSFS lavas (Ce/Pb ≥ 2l, Ba/Nb ≤ l0 and MgO ≥ 8 wt %). The continuous curves show non-modal batch melting models for a lherzolite (with a primitive mantle composition) and a hornblendite metasomatic vein (AG4 of Pilet *et al.*, 2008) as starting materials, from 1 to l6·8% and from 25 to 60% melting respectively. The kink in the metasomatic vein melting curve results from complete consumption of amphibole at 47·5% melting; beyond this point, melting mode of the residual "pyroxenite" vein is assumed to be modal for simplicity. It should be noted that most basalt samples fall in the grey-shaded fields, which define the possible melt compositions from 0 to l00% mixing of small-degree ($F = 2$–10%) lherzolite melts and large-degree ($F = 30$–45%) metasomatic vein melts. For clarity in the diagram, the degrees of melting and mixing are not always displayed but the latter can be evaluated from the representative mixing curve (dashed) between a 6% lherzolite melt and a 40% vein melt (numbers along the dashed curve denote the proportion of lherzolite melt in the hybrid melt). Italic numbers along the continuous curves are the degrees of partial melting. Despite some scatter, samples of the Al Ghab group (mainly basanites) are characterized by higher $(La/Yb)_N$, $(Dy/Yb)_N$ and $(Sm/Zr)_N$, and lower $(K/La)_N$ and $(Rb/Ba)_N$, suggesting greater influence of metasomatic veins during their petrogenesis. Positions of the terms basanite, alkali basalt (AB) and tholeiitic basalt (TB) along the top of (a) and (b) denote the approximate $(La/Yb)_N$ ranges of each type. Other parameters are given in Table 6 and described in the text. Primitive mantle normalizing values are from McDonough & Sun (1995). *F*, degree of partial melting.

magmas, the magmas may be considered rather primitive. This is consistent with the above conclusion that many of these magmas probably did not stagnate for long at crustal levels but ascended to the surface rapidly, as they contain mantle xenoliths and appear to be free from crustal contamination.

Magma genesis beneath the northern DSFS region

Insight from trace element variations

Insight into the source mineralogy of the N-DSFS lavas can be gained from the primitive mantle normalized trace element patterns of the most primitive samples. The general patterns for the Al Ghab group and the Homs group are similar, but there are significant variations in K/La (K-anomaly), Rb/Ba (Rb-anomaly) and, to a lesser extent, Sm/Zr (Zr-anomaly) that are correlated with variations of La/Yb (Fig. l0) and Si_{10} [element fractionation-corrected to l0 wt % MgO following the methods of Klein & Langmuir (l987); Fig. l1]. In detail, high La/Yb samples (mainly the Al Ghab group) are associated with low Si_{10}, K/La and Rb/Ba, and high Ti_{10} and Sm/Zr, and vice versa for the low La/Yb samples (most of the Homs samples). Krienitz *et al.* (2007) contended that low K/La might be a compositional feature of the mantle source beneath southern Syria; however, we stress that the important question is how the element pair K–La can be effectively fractionated from each other whilst they are similarly incompatible in a simple peridotite assemblage (ol + cpx + opx + grt/spl). This concern leads to another interpretation for the negative K/La–La/Yb correlation; that is, that K was held back relative to other very

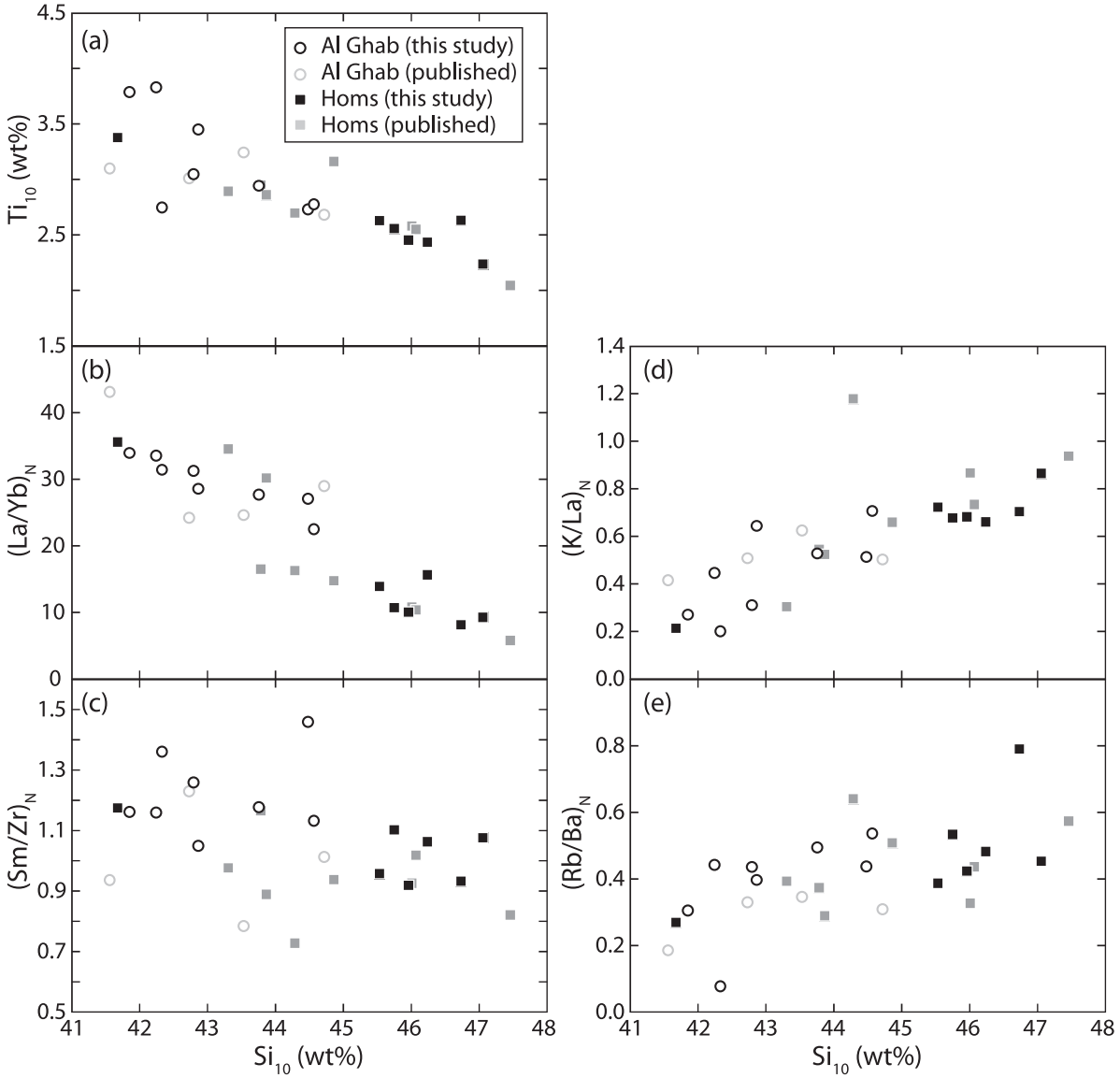

Fig. 11. (a) Ti_{10}, (b) $(La/Yb)_N$, (c) $(Sm/Zr)_N$, (d) $(K/La)_N$ and (e) $(Rb/Ba)_N$ vs Si_{10} for the relatively primitive N-DSFS samples ($Ce/Pb \geq 21$, $Ba/Nb \leq 10$ and pre-fractionation-corrected $MgO \geq 8$ wt %). Ti_{10} and Si_{10} are the estimated concentrations of TiO_2 and SiO_2 respectively at 10 wt % MgO after correction for crystal fractionation following the method of Klein & Langmuir (1987). Primitive mantle normalizing values are from McDonough & Sun (1995).

incompatible elements by amphibole or phlogopite in the mantle source during partial melting (e.g. le Roex *et al.*, 2001; Späth *et al.*, 2001; Haase *et al.*, 2004; Johnson *et al.*, 2005; Thompson *et al.*, 2005; Weinstein *et al.*, 2006; Sprung *et al.*, 2007; Chang *et al.*, 2009). This explanation, however, does not appear to be capable of accounting for the systematic variations of Sm/Zr and Rb/Ba with La/Yb. Although both Rb and Ba are compatible in phlogopite with $D_{Rb}^{phlog/melt} > D_{Ba}^{phlog/melt}$ (Adam & Green, 2006), which can result in a positive Rb/Ba–La/Yb relationship in magmas, there is a large variation of Sm/Zr (about twofold variation) within the observed N-DSFS magmas that cannot be attributed to the presence of phlogopite, in which Sm and Zr are highly incompatible during partial melting (Adam & Green, 2006). Likewise, Zr, Sm, Rb and Ba are incompatible in amphibole (LaTourrette *et al.*, 1995), suggesting that amphibole is also unlikely to generate such elemental variations. Rather we suggest that the correlations between K/La, Sm/Zr and Rb/Ba (and also Ti_{10} and Dy/Yb, which are discussed below) with La/Yb and Si_{10} can be interpreted as mixing lines whose end-members are yet to be defined.

Insight from SiO_2 contents

The most primitive N-DSFS magmas (MgO > 8 wt %) exhibit an appreciable range of SiO_2 contents from ~41 to 48 wt % (from basanites to alkali basalts transitional to tholeiitic basalts); this range does not change very much after fractionation correction (Fig. 11). Although the depth and to a lesser extent the degree of partial melting are known to exert some control on the SiO_2 contents of magmas (e.g. Hirose & Kushiro, 1993; Kushiro, 1996; Walter, 1998; Wasylenki *et al.*, 2003), low-Si magmas have never been successfully produced in partial melting experiments of anhydrous peridotite (S. Pilet, personal communication); experimental partial melts of anhydrous peridotite are mostly in the range 45–54 wt % SiO_2 (e.g. Hirose & Kushiro, 1993; Kushiro, 1996; Walter, 1998; Wasylenki *et al.*, 2003). The presence of phlogopite (deductively also amphibole) in a peridotitic source does not seem to lower the SiO_2 contents of the melts either, as evidenced by the experiments of Mengel & Green (1989). It is clear that whereas the N-DSFS alkali and tholeiitic basalts can be products of peridotite melting, the basanites cannot.

In recent years, carbonated Si-deficient eclogite (Dasgupta *et al.*, 2006) and lightly carbonated peridotite (Dasgupta *et al.*, 2007) have been considered plausible sources of contributing components to (highly) Si-undersaturated melts. The latter especially has been supported on theoretical and experimental grounds, which suggest that the presence of CO_2 in the mantle can stabilize orthopyroxene, preventing its entry into the melt, and giving rise to Si-poor liquids. Nevertheless, there are compositional components of these carbonated melts that do not fit the compositional spectrum of OIB. Most notably, CO_2-bearing eclogite tends to generate too high FeO, CaO and CaO/Al_2O_3, and CO_2-bearing peridotite too low FeO and SiO_2, and too high CaO and CaO/Al_2O_3. The K_2O contents of the melts that have been generated in both types of experiment are also very low, in contrast to the generally high alkali contents of Si-undersaturated basalts. Although Dasgupta *et al.* (2007) infer that by reducing the CO_2 content in the peridotite to ~0·1–0·25 wt % and limiting the degree of partial melting to 1–5%, sources with a primitive mantle composition might be capable of yielding basaltic melts with SiO_2 and CaO contents similar to those observed in alkali (ne-normative) OIB (and thus those of the N-DSFS magmas), actual experiments are still not available to verify this. It was also argued (Prytulak & Elliott, 2007) that primitive mantle is too Ti-poor to explain the high-Ti characteristics of most alkali OIB; increasing the Ti and alkali content of the source may imply a metasomatized or non-peridotitic source, such as hornblendite.

Judging from these results, we consider hornblendite or similar amphibole-rich veins to be by far the most plausible source of, or contributing component to, the N-DSFS basanitic magmas and perhaps most Si-undersaturated magmas in general. In the experiments conducted at 1·5 GPa, Pilet *et al.* (2008) obtained partial melts of hornblendite (AG4) and sandwiched hornblendite–moderately depleted peridotite (DMM1), which are comparable in major and trace element compositions with alkali OIB. A major finding from these experiments is that these lithologies, because of the low-solidus temperature of hornblendite, melt in large fractions, and for this reason the melts generated inherit many of the source's compositional features. These melts have high alkalis and TiO_2 and, on primitive mantle normalized trace element diagrams, exhibit negative anomalies of Rb, K, Pb and Zr, with reasonably high LREE/heavy REE (HREE) (e.g. La/Yb) and middle REE (MREE)/HREE (e.g. Dy/Yb). All these characteristics reflect what we have observed for the N-DSFS magmas, particular the most Si-undersaturated examples (Figs 10 and 11).

Lithospheric and sub-lithospheric mantle interactions: semi-quantitative constraints

Using current knowledge of trace element partition coefficients, the partial melting conditions under which the parental N-DSFS magmas were generated can be modelled and our hypothesis that the compositional spectrum of the N-DSFS magmas resulted from mixing between hornblendite and peridotite melts can be tested. In the following discussion, only lavas with ≥8 wt % MgO are used as they are considered to have retained a sufficient trace of their melting history.

Varying negative K-, Zr- and Rb-anomalies in correlation with La/Yb are considered. Co-variation between Dy/Yb and La/Yb is also considered to constrain the involvement of garnet in the source. All partial melting calculations for the model presented in Fig. 10 and Table 6 have been performed assuming batch, non-modal incongruent melting (Shaw, 1970; Zou, 2007). Compositions of the source components, peridotite and hornblendite, are those of primitive mantle (McDonough & Sun, 1995) and the AG4 hornblendite (from the French Pyrenees), respectively. The latter was selected because it contains amphiboles typical of those in hydrous veins from the oceanic and continental lithosphere and had been the subject of previous partial melting experiments (Pilet *et al.*, 2007, 2008). For the peridotite component, using a depleted mantle composition (e.g. Workman & Hart, 2005) or a spinel-facies peridotite with a primitive mantle composition cannot reproduce the moderately high $(Dy/Yb)_N$ (>1·6) and $(La/Yb)_N$ (>5), and the limited range of Yb_N (3·0–4·3) of the Homs tholeiitic and alkali basalts. Although Blundy *et al.* (1998) found that HREE may also be compatible in clinopyroxene on the spinel-facies lherzolite solidus, their experiments yielded $D^{cpx/melt}_{MREE}$ not significantly different from $D^{cpx/melt}_{HREE}$ [e.g. $D^{cpx/melt}_{Gd}/D^{cpx/melt}_{Lu} \approx 0{\cdot}67$; compared with $D^{grt/melt}_{Gd}/D^{grt/melt}_{Lu} \approx 0{\cdot}02$–$0{\cdot}11$

Table 6: Mineral–melt partition coefficients, source compositions and source modes used in partial melting forward modelling

	Partition coefficient						Abundance (ppm)	
	Ol	Opx	Cpx	Spl	Grt	Amph	PM	Amph vein[13]
Rb	0·00018[1]	0·0038[4]	0·015[5]	0·029[5]	0·002[4]	0·141[9]	0·6	7
Ba	0·00014[2]	0·0036[4]	0·00068[6]	0·0006[5]	0·002[4]	0·16[10]	6·6	384
K	0·000000001[3]	0·00001[3]	0·0072[6]	0[3]	0·013[7]	1·36[11]	240	10137
Zr	0·0005[3]	0·014[3]	0·1234[6]	0·07[3]	0·39[7]	0·13[10]	10·5	211
La	0·000007[3]	0·0005[3]	0·0536[6]	0·0006[3]	0·0018[7]	0·117[9]	0·648	52·7
Sm	0·0007[3]	0·02[3]	0·291[6]	0·0006[3]	0·23[7]	0·756[12]	0·406	12·2
Dy	0·004[3]	0·06[3]	0·442[6]	0·0015[3]	1·92[8]	0·899[9]	0·674	7
Yb	0·023[3]	0·1[3]	0·43[6]	0·0045[3]	5·14[7]	0·684[9]	0·441	2·54

	Source mode[16]					
	Ol	Opx	Cpx	Spl	Grt	Amph
Grt-bearing lherzolite						
Mineral mode	0·56	0·25	0·14		0·05	
Melting mode[14]	0·07	−0·16	0·68		0·25	
Grt-bearing amph metasomatic vein						
Mineral mode	0	0	0	0	0·05	0·95
Melting mode[15]	0	0	−0·34	0	−0·16	1

Ol, olivine; Opx, orthopyroxene; Cpx, clinopyroxene; Spl, spinel; Grt, garnet; Amph, amphibole; PM, primitive mantle of McDonough & Sun (1995).
Sources: 1, McKenzie & O'Nions (1991); 2, calculated using the algorithms of Bédard (2005) assuming 12 wt % MgO in the melt; 3, Kelemen *et al*. (1993); 4, Adam & Green (2006); 5, Elkins *et al*. (2008); 6, Hart & Dunn (1993); 7, van Westrenen *et al*. (2000); 8, calculated with respect to $D_{Yb}^{grt/melt} = 5{\cdot}14$ (van Westrenen et al., 2000) using equation (3) of Blundy & Wood (1994); 9, calculated using the algorithms of Tiepolo *et al*. (2007) assuming $X_{nf}/X = 0{\cdot}56$; 10, LaTourrette *et al*. (1995); 11, Dalpé & Baker (1994); 12, calculated using the algorithms of Tiepolo *et al*. (2000) assuming $X_{nf}/X = 0{\cdot}56$; 13, hornblendite AG4 (Pilet *et al*., 2008); 14, Walter (1998); 15. S. Pilet (personal communication).
[16]Negative values of melting modes denote minerals are producing during partial melting.

(Green *et al*., 2000)]. Such a small difference is not capable of generating the high Dy/Yb observed in the Homs magmas.

It should be noted that the use of a primitive mantle composition does not imply that the source is primordial mantle. The Homs samples exhibit relatively low $^{86}Sr/^{87}Sr$ and high $^{143}Nd/^{144}Nd$ ratios compared with the Bulk Earth, requiring long-term depletion in the source. Therefore this primitive mantle composition must reflect an originally depleted but subsequently re-fertilized mantle source, presumably enriched by incompatible element-rich fluids or melts to a near-primitive mantle composition.

For the hornblendite component, a garnet-bearing assemblage is required, given the limited range of Yb_N (3·4–4·8) and very high $(Dy/Yb)_N$ (up to 2·5) of the N-DSFS basanites. Although spinel-bearing hornblendites are more common in nature, garnet amphibole veins have been reported in the French Pyrénées (Lorand & Gregoire, 2010, and references therein). Hornblendite melting experiments have yielded melts, at 1250°C and 2·5 GPa (~30% of melting), with $(La/Yb)_N$ over 36 (S. Pilet, unpublished data), which is similar to the highest $(La/Yb)_N$ of the N-DSFS lavas.

In the model set out in Fig. 10, the peridotite and hornblendite melting curves, as expected, cannot alone reproduce the variations of the N-DSFS samples. The samples fall between the two curves and can be interpreted as products of varying degrees of mixing (the shaded region in Fig. 10) between 2–10% melt fractions of peridotite and

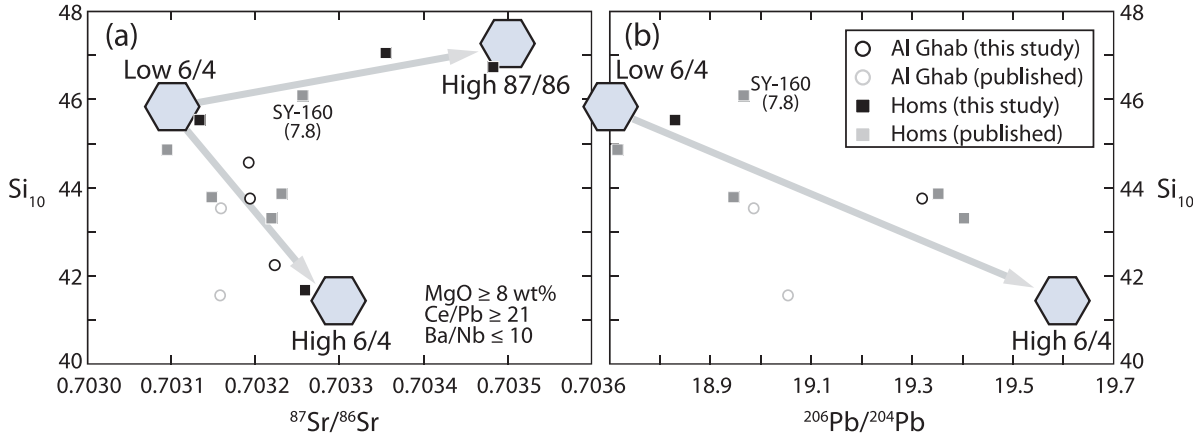

Fig. 12. Si_{10} (wt %) vs (a) $^{87}Sr/^{86}Sr$ (a) and (b) $^{206}Pb/^{204}Pb$ for the relatively primitive N-DSFS samples (Ce/Pb ≥ 21, Ba/Nb ≤ 10 and pre-fractionation-corrected MgO ≥ 8 wt %). The shaded hexagons denote the positions of the three inferred isotopic end-member components, the low 6/4 component, the high 6/4 component and the high 87/86 component, described in the text and in Table 5. These inferred components appear to reside in different sources, which eventually contributed to distinct geochemical characteristics (e.g. SiO_2) in the resultant melts (see text). One published data point, SY-160 (Krienitz *et al.*, 2009), with 7·8 wt % MgO is also included for comparison. Primitive mantle normalizing values are from McDonough & Sun (1995).

30–45% melt fractions of hornblendite, with the Homs group containing a more significant peridotite component (>75%; see the reference mixing curves in Fig. 10). The model also suggests a contribution of ~40–60% (up to 80%) amphibole metasomatic veins in the source of the N-DSFS basanites. This is in accord with Pilet *et al.*'s (2008) findings that partial melts of hornblendite are highly Si-undersaturated, nephelinitic liquids, which upon reactions with the surrounding lherzolite can produce basanites and alkali basalts.

In light of the results of the hornblendite melting experiments, the actual melting that generated the N-DSFS magmas may have been more complicated than the simple melt mixing model presented in Fig. 10. The reason is that once highly Si-undersaturated melts are produced by melting of the hornblendite veins, the melts react with the wall-rock, dissolving orthopyroxene, thereby increasing the SiO_2 content and diluting the trace element content of the melts (Pilet *et al.*, 2008, 2010, and references therein). This leads to a re-evaluation of the observed range of SiO_2 (as well as TiO_2, La/Yb, Dy/Yb, K/La, Rb/Ba, Sm/Zr and many other geochemical features) of the N-DSFS magmas—the range can be interpreted as a result of (1) dissolution of orthopyroxene from the wall-rock peridotite owing to melt–rock reaction, or (2) mixing of melts derived from two independent sources, such as metasomatic veins (for the low-SiO_2 melts) vs plume or asthenosphere (for the high-SiO_2 melts).

The observation that there are at least three isotopic components (the low 6/4 component, the high 6/4 component and the high 87/86 component; Table 5) in the source of the N-DSFS lavas seems to suggest that both scenarios were operating during the genesis of the magmas. The relationship is clear on plots of Si_{10} against isotopic composition (e.g. $^{87}Sr/^{86}Sr$ and $^{206}Pb/^{207}Pb$; Fig. 12). The amphibole metasomatic vein component, which is important in the source of the low-SiO_2 lavas, has high $^{206}Pb/^{207}Pb$ and moderately low $^{87}Sr/^{86}Sr$ (the high 6/4 component). The highest SiO_2 and $^{87}Sr/^{86}Sr$ lavas (the high 87/86 component) may result from melting of the sub-lithospheric mantle (?asthenosphere or plume). Those lavas with the lowest $^{87}Sr/^{86}Sr$ and $^{206}Pb/^{207}Pb$ at moderately high SiO_2 (the low 6/4 component) may reflect melting of the lithospheric peridotite wall-rock, which hosts the metasomatic veins. The lowering of SiO_2 in the low 6/4 component compared with the high 87/86 component is consistent with melt derivation via (1) assimilation and reaction with Si-undersaturated melts that came from the metasomatic veins and/or (2) melting of a modally metasomatized lithology (e.g. amphibole- or phlogopite-bearing peridotite), which is likely for a wall-rock peridotite (e.g. Harte *et al.*, 1993; Witt-Eickschen *et al.*, 2003).

In Fig. 12, the Homs group comprises all three components, whereas the Al Ghab group comprises samples lying only between the low 6/4 component and the high 6/4 component. If the high 87/86 component can be interpreted, as above, as a sub-lithospheric mantle component, the absence of the high 87/86 component for the Al Ghab samples may imply that these magmas were generated within the lithospheric mantle, whereas the Homs magmas involved the participation of both lithospheric and sub-lithospheric source materials. The slight distinction of the Al Ghab samples from the majority in Fig. 12 may reflect isotopic heterogeneity between the amphibole

metasomatic vein components of the Al Ghab and Homs regions. Further defining this is, however, hindered by the limited data available for the Al Ghab group.

Role of hydrous metasomatic veins in inciting mantle melting

The hydrous nature of the western Arabian mantle, as proposed here and elsewhere (e.g. Stein *et al.*, 1997; Weinstein *et al.*, 2006), is supported by the occurrence of hydrous, modally metasomatized mantle xenoliths, and amphibole-rich cumulate xenoliths and amphibole megacrysts, which could be fragments of metasomatic veins (McGuire, 1988; Henjes-Kunst *et al.*, 1990; Blusztajn *et al.*, 1995; Sharkov *et al.*, 1996; Nasir & Safarjalani, 2000; Turkmani, 2000; Baker *et al.*, 2002; Downes *et al.*, 2004; Kaliwoda, 2004; Turkmani & Al-Shara'a, 2004; Kaliwoda *et al.*, 2007; Ismail *et al.*, 2008; Nasir & Rollinson, 2009; G. Ma *et al.*, unpublished data). On the contrary, Krienitz *et al.* (2009) argue against the existence of a hydrous lithospheric source beneath northwestern Arabia, and propose that the negative K anomalies seen in the Syrian basalts are an intrinsic source feature that resides within the asthenospheric mantle because similar negative K anomalies are also present in some Red Sea basalts. However, the Red Sea samples that have low K/La also have higher $(La/Sm)_N$ (see fig. 9b of Krienitz *et al.*, 2009). This K/La vs $(La/Sm)_N$ plot is analogous to the $(K/La)_N$ vs $(La/Yb)_N$ (Fig. 10a) plot in this study, and a negative correlation has been shown to reflect the varying extent of metasomatic vein and peridotite wall-rock interactions, with or without involvement of sub-lithospheric peridotite mantle. In addition, the low K/La, high $(La/Sm)_N$ Red Sea samples (e.g. Altherr *et al.*, 1988) that Krienitz *et al.* (2009) referred to are not ordinary MORB tholeiites, but alkali basalts (OIB) sampled directly from seamounts or volcanic islands (i.e. Zubair Island Group) adjacent to the Red Sea spreading centre. These Red Sea OIB are more likely to be low-degree partial melts that were generated from the asthenospheric or lithospheric peridotite mantle, or laterally migrating Afar mantle plume, and that reacted with the lithospheric metasomatic veins. As Niu (2008, 2009) and Humphreys & Niu (2009) advocate, H_2O- and CO_2-rich incipient melts may exist in the seismic low velocity zone (LVZ) of the upper mantle (asthenosphere). Upward migration of these melts owing to their buoyancy will form a melt-rich layer atop the LVZ and metasomatize the base of the lithosphere. In detail, the hydrous melts evolve during migration within the lithosphere and produce metasomatic vein lithologies, such as hornblendites, examples of which have been reported in mantle xenoliths from northwestern Syria and Israel (Downes *et al.*, 2004; G. Ma *et al.*, unpublished data). The vein lithologies form by fractional crystallization of a continuum of phase assemblages, from anhydrous (pyroxene + garnet ± olivine) to hydrous (pyroxene + amphibole ± phlogopite), that are enriched in highly incompatible elements (Morris & Pasteris, 1987; Harte *et al.*, 1993; Pilet *et al.*, 2010). A similar model might be applied to the Arabian continental lithosphere, with the formation of metasomatic lithologies related to the growth of the lithosphere during Late Proterozoic times or during later intraplate magmatism that did not necessarily 'penetrate' the entire lithosphere.

The solidi of hydrous peridotite lithologies have been shown in numerous experimental studies (e.g. Niida & Green, 1999, and the references therein) to be ~150–300°C lower than the anhydrous peridotite solidus at similar pressures. Pilet *et al.* (2008) determined the solidus of hornblendite at ~1150°C (at 1·5 GPa) to be ~180°C lower than that of anhydrous depleted peridotites at the same pressure (Hirschmann, 2000; Wasylenki *et al.*, 2003). They further show that reaction melts between the hornblendite and peridotite could be generated >100°C below the expected anhydrous solidus temperature of the peridotite. A strong implication of these experimental findings is that Si-undersaturated magmas like those from the N-DSFS could be generated without much thermal perturbation. This relatively 'cold' melting scenario is consistent with the observations that there is no significant crustal domal uplift or large igneous province (LIP) associated with the Late Cenozoic volcanism in the Levant region.

Cause of mantle melting and implications for regional tectonomagmatism

Our proposed model incorporates varying extents of melting and interaction of hornblendite metasomatic veins, wall-rock lithospheric peridotite and sub-lithospheric peridotite in the genesis of the N-DSFS basanites, alkali basalts and tholeiitic basalts. This shares some similarities with the model of Weinstein *et al.* (2006) for the genesis of similar magma types in the Golan Heights further to the south. In their model, alkali basaltic melts are produced by partial melting of a garnet-bearing amphibole peridotite that had undergone partial dehydration, whereas the basanitic melts are generated by partial melting of garnet–amphibole pyroxenite veins that formed as a result of partial melting of amphibole peridotite, followed by complete solidification and dehydration. Weinstein *et al.* (2006) further suggested that the compositional spectrum (basanite to alkali basalt) of the volcanic rocks from the Golan Heights was a result of binary mixing between melts generated from these two sources.

There is increasing dominance of basanites over alkali (and tholeiitic) basalts from south (Homs; latest Miocene–Early Pliocene) to north (Al Ghab; Late Pliocene–Quaternary) over time. This feature has also been observed for basalts erupting in the Golan Heights and has been attributed to the heterogeneous distribution of vein-rich and vein-poor domains within the Golan mantle lithosphere (Weinstein *et al.*, 2006). However, in Syria the south to north increase in basanite dominance is

accompanied by a significant decrease in the overall volume of magma erupted (Fig. 1). These characteristics may therefore be more consistent with a diminished thermal perturbation (see below) below the Al Ghab volcanic field during Late Pliocene to Quaternary times.

To trigger partial melting beneath the N-DSFS region, either lithospheric extension or a heat source is required, despite the low solidus temperatures of the hydrous metasomatic veins and their mixtures with peridotites. Although large-scale sedimentary basins denoting significant lithospheric extension are widespread along the Levantine coast of Arabia (e.g. Galilee–Yizre'el Valley and Wadi Sirhan (south of Damascus; e.g. Matmon *et al.*, 2003), many of these features pre-date (Early and Mid-Miocene) the Syrian N-DSFS volcanic fields and are found further to the south. Latest Miocene–Quaternary extensional features associated with the N-DSFS volcanism are simply localized pull-apart basins (e.g. Al Ghab Depression; Brew *et al.*, 2001*b*) that resulted from sinistral movements along the DSFS. The DSFS therefore appears to be a structure that confines volcanic eruption rather than directly incites mantle melting. A heat source appears to be necessary to initiate melting.

Two existing models are discussed here: (1) convective flow of actively upwelling asthenospheric mantle material that was channelled and flowed northwards along a pre-existing regional flexure in the Arabian lithosphere; (2) emplacement of separate mantle plumes, which Camp & Roobol (1992) used to explain the south-to-north migration of Late Cenozoic volcanism in Saudi Arabia. In Syria, the observation that the northward migration of the volcanism was contemporaneous with the propagation of the DSFS and accompanied by an increase in Si-undersaturation in magma chemistry and a decrease in magma volume appears to be more consistent with a channelled flow model. When upwelling mantle material was first emplaced beneath the Homs region in the latest Miocene, it was at its hottest and itself melted adiabatically to contribute rising magmas (the sub-lithospheric component identified above—the high 87/86 component). Heat advection and conduction caused the lithosphere to melt; interactions involving wall-rock assimilation (metasomatic veins and lithospheric peridotite assimilated by the ascending, hot sub-lithospheric melts) or melt hybridization (melts formed separately at first and mixed during ascent through the crust) produced a spectrum of magmas from basanite to tholeiitic basalt. Northward propagation of the DSFS diverted the partially molten sub-lithospheric material, which might have been continuously rising beneath the Homs region, to the Al Ghab region in the Late Pliocene. This material was probably cooler than it had been, and was unable to penetrate the Al Ghab lithosphere. The amount of thermal perturbation by conduction was probably just sufficient to trigger melting of the lowest solidus materials within the base of the lithosphere, the amphibole-bearing metasomatic veins, which interacted with their wall-rock lithospheric peridotite to produce a spectrum of basanites and alkali basalts.

Given the distance between Syria and Saudi Arabia, but overlap of the volcanic episodes (6–1 Ma for Syria vs 12 Ma–Recent for Saudi Arabia), we propose that the thermal perturbation came from a single zone of asthenospheric upwelling beneath the Homs volcanic field, rather than a northward continuation of Saudi Arabian channelled flow (Camp & Roobol, 1992), which has been considered to originate from the Afar plume rising beneath Yemen and Ethiopia. The upwelling may be a small-scale mantle diapir (or convective instability) similar to those suggested by Wilson & Patterson (2001) to be the cause of Cenozoic volcanism in Europe, or passive asthenospheric upwelling resulting from slab steepening and subsequent break-off beneath eastern Anatolia (Keskin, 2003; Sengör *et al.*, 2003; Krienitz *et al.*, 2006; see also the review of Keskin, 2007).

The above interpretations are supported by both regional and local geophysical studies. Debayle *et al.* (2001) demonstrate the existence of a broad low-velocity seismic anomaly at a depth of 100 km beneath much of Arabia, attesting to the presence of a widespread thermal anomaly or a partially molten mantle. In a more local study, Park *et al.* (2007) presented tomographic images delineating a NW–SE-trending low-velocity feature beneath the western side of the Arabian Shield, comparable with the channelled flow model described by Camp & Roobol (1992). This anomaly, however, does not reach northwestern Arabia but is confined beneath the Red Sea coast in Saudi Arabia (south of ~27°N). It appears that Cenozoic Arabia has been affected by various asthenospheric upwellings and that each of these might have resulted in lateral flow of asthenospheric material channelled at the base of the lithosphere along pre-existing or developing linear lithospheric structures (Camp & Roobol, 1992; Weinstein *et al.*, 2006; Krienitz *et al.*, 2009; see also Sleep, 2008).

CONCLUDING REMARKS

Latest Miocene–Quaternary continental volcanism occurring in the vicinity of the Syrian N-DSFS forms two suites. The older (~6–4 Ma), Homs volcanic group comprises basanite, alkali basalt and tholeiitic basalt, whereas the younger (~4–1 Ma), Al Ghab volcanic group comprises mainly basanite and subordinate amounts of hawaiite and alkali basalt.

The petrography, mineral chemistry and bulk-rock major and trace element compositions of the lavas are consistent with those of magmas that have undergone varying amounts of olivine ± clinopyroxene ± spinel fractionation, with feldspar fractionation encountered only in the most evolved lavas. Some lavas have additionally been affected by olivine ± clinopyroxene phenocryst accumulation.

The major and trace element and Nd–Sr–Pb isotopic compositions of the basalts cannot be explained only by crystal fractionation, and therefore reflect both source heterogeneity and minor amounts of upper crustal contamination. Such contamination can be explained by ≤6% assimilation of Late Proterozoic Arabian Shield material via AFC processes during ascent of the magmas.

Among the least contaminated samples, the Si-undersaturated lavas (basanites) are characterized by low SiO_2, K/La and Rb/Ba, and high TiO_2, Sm/Zr and Dy/Yb. These features are consistent with magma derivation largely from garnet-bearing hornblendite metasomatic veins, plus modest interactions with the surrounding wall-rock peridotite within the lithospheric mantle. The increasing extent of interaction and hybridization of such veins or their melted products with the wall-rock peridotite and rising asthenospheric magmas generated the more Si-rich N-DSFS lavas (alkali and tholeiitic basalts).

The observation that the younger Al Ghab group is dominated by basanites and the older Homs group by alkali and tholeiitic basalts reveals a significant control on magma compositions by hornblendite metasomatic veins and peridotitic mantle, respectively, during magma genesis. The temporal, spatial and compositional variations of the N-DSFS basalts can be explained as a consequence of the northward propagation of the N-DSFS during the Late Cenozoic and consequent channelling at the base of the lithosphere of upwelling asthenospheric mantle from the Homs region.

ACKNOWLEDGEMENTS

Many thanks go to Luis Castano, Ahmed Merhej, Mike Searle and Barry Wood for their invaluable effort in supporting G.S.K.M in Syria; to Mei-fu Zhou for his invaluable support; and to Al-Sallakh Mohammad for field assistance. Lin-li Chen, Xiao Fu, Jin-long Ma and Simon Leung are gratefully acknowledged for their help during analytical work. Special thanks go to the General Establishment of Geology and Mineral Resources, Syria, particularly to Morwan Al-Shara'a, Abdulsalam Turkmani, Tamam Darouz and Nouh Wappy, and to Maurel & Prom Syria for logistic and financial support in fieldwork. We are grateful to Hilary Downes, Karsten Haase, Sébastien Pilet, Ian Smith, Yishai Weinstein and an anonymous reviewer for their constructive reviews of the paper. Continuous discussion with S. Pilet was stimulating and beneficial.

FUNDING

This work was supported by research funds provided by HKU (grant numbers 200607176152 and 200807176091 to J.M.).

SUPPLEMENTARY DATA

Supplementary data for this paper are available from *Journal of Petrology* online.

REFERENCES

Abdel-Rahman, A.-F. M. & Nassar, P. E. (2004). Cenozoic volcanism in the Middle East: petrogenesis of alkali basalts from northern Lebanon. *Geological Magazine* **141**, 545–563.

Adam, J. & Green, T. H. (2006). Trace element partitioning between mica- and amphibole-bearing garnet lherzolite and hydrous basanitic melt: 1. Experimental results and the investigation of controls on partitioning behaviour. *Contributions to Mineralogy and Petrology* **152**, 1–17.

Altherr, R., Henjes-Kunst, F., Puchelt, H. & Baumann, A. (1988). Volcanic activity in the Red Sea axial trough—evidence for a large mantle diapir? *Tectonophysics* **150**, 121–133.

Altherr, R., Henjeskunst, F. & Baumann, A. (1990). Asthenosphere versus lithosphere as possible sources for basaltic magmas erupted during formation of the Red Sea: constraints from Sr, Pb and Nd isotopes. *Earth and Planetary Science Letters* **96**, 269–286.

Baker, J., Chazot, G., Menzies, M. & Thirlwall, M. (1998). Metasomatism of the shallow mantle beneath Yemen by the Afar plume—implications for mantle plumes, flood volcanism, and intraplate volcanism. *Geology* **26**, 431–434.

Baker, J., Chazot, G., Menzies, M. A. & Thirlwall, M. (2002). Lithospheric mantle beneath Arabia: a Pan-African protolith modified by the Afar and older plumes, rather than a source for continental flood volcanism? In: Menzies, M. A., Klemperer, S. L., Ebinger, C. J. & Baker, J. (eds) *Volcanic Rifted Margins Geological Society of America, Special Papers* **362**, 65–80.

Bartov, Y., Steinitz, G., Eyal, M. & Eyal, Y. (1980). Sinistral movement along the Gulf of Aqaba: its age and relation to the opening of the Red Sea. *Nature* **285**, 220–222.

Bédard, J. H. (2005). Partitioning coefficients between olivine and silicate melts. *Lithos* **83**, 394–419.

Bertrand, H., Chazot, G., Blichert-Toft, J. & Thoral, S. (2003). Implications of widespread high-μ volcanism on the Arabian Plate for Afar mantle plume and lithosphere composition. *Chemical Geology* **198**, 47–61.

Blundy, J. D., Robinson, J. A. C. & Wood, B. J. (1998). Heavy REE are compatible in clinopyroxene on the spinel lherzolite solidus. *Earth and Planetary Science Letters* **160**, 493–504.

Blundy, J. D. & Wood, B. J. (1994). Prediction of crystal–melt partition coefficients from elastic moduli. *Nature* **374**, 452–454.

Blusztajn, J., Hart, S. R., Shimizu, N. & McGuire, A. V. (1995). Trace-element and isotopic characteristics of spinel peridotite xenoliths from Saudi Arabia. *Chemical Geology* **123**, 53–65.

Bogaard, P. J. F. & Wörner, G. (2003). Petrogenesis of basanitic to tholeiitic volcanic rocks from the Miocene Vogelsberg, Central Germany. *Journal of Petrology* **44**, 569–602.

Brew, G., Barazangi, M., Al-Maleh, A. K. & Sawaf, T. (2001*a*). Tectonic and geologic evolution of Syria. *GeoArabia* **6**, 573–616.

Brew, G., Lupa, J., Barazangi, M., Sawaf, T., Al-Imam, A. & Zaza, T. (2001*b*). Structure and tectonic development of the Ghab Basin and the Dead Sea fault system, Syria. *Journal of the Geological Society, London* **158**, 665–674.

Camp, V. E. & Roobol, M. J. (1992). Upwelling asthenosphere beneath western Arabia and its regional implications. *Journal of Geophysical Research* **97**, 15225–15271.

Çapan, U. Z., Vidal, P. & Cantagrel, L. M. (1987). K–Ar, Nd, Sr and Pb isotopic study of Quaternary volcanism in Karasu Valley (Hatay), N end of Dead Sea rift zone in SE Turkey. *Yerbilimleri* **14**, 165–178.

Chang, J. M., Feeley, T. C. & Deraps, M. R. (2009). Petrogenesis of basaltic volcanic rocks from the Pribilof Islands, Alaska, by melting of metasomatically enriched depleted lithosphere, crystallization differentiation, and magma mixing. *Journal of Petrology* **50**, 2249–2286.

Dalpé, C. & Baker, D. R. (1994). Partition coefficients for rare-earth elements between calcic amphibole and Ti-rich basanitic glass at 1·5 GPa, 1100°C. *Mineralogical Magazine* **58A**, 207–208.

DePaolo, D. J. (1981). Trace element and isotopic effects of combined wallrock assimilation and fractional crystallization. *Earth and Planetary Science Letters* **53**, 189–202.

Dasgupta, R., Hirschmann, M. M. & Stalker, K. (2006). Immiscible transition from carbonate-rich to silicate-rich melts in the 3 GPa melting interval of eclogite + CO_2 and genesis of silica-undersaturated ocean island lavas. *Journal of Petrology* **47**, 674–671.

Dasgupta, R., Hirschmann, M. M. & Smith, N. D. (2007). Partial melting experiments of peridotite CO_2 at 3 GPa and genesis of alkalic ocean island basalts. *Journal of Petrology* **48**, 2093–2124.

Debayle, E., Lévêque, J.-J. & Cara, M. (2001). Seismic evidence for a deeply rooted low-velocity anomaly in the upper mantle beneath the northeastern Afro/Arabian continent. *Earth and Planetary Science Letters* **193**, 423–436.

DePaolo, D. J. (1988). *Neodymium Isotope Geochemistry: an Antroduction*. New York: Springer.

Downes, H., Beard, A. & Hinton, R. (2004). Natural experimental charges: an ion-microprobe study of trace element distribution coefficients in glass-rich hornblendite and clinopyroxenite xenoliths. *Lithos* **75**, 1–17.

Elkins, L. J., Gaetani, G. A. & Sims, K. W. W. (2008). Partitioning of U and Th during garnet pyroxenite partial melting: Constraints on the source of alkaline ocean island basalts. *Earth and Planetary Science Letters* **265**, 270–286.

Eyal, M., Eyal, Y., Bartov, Y. & Steinitz, G. (1981). The tectonic development of the western margin of the Gulf of Elat (Aqaba) Rift. *Tectonophysics* **80**, 39–66.

Falloon, T. J., Green, D. H., O'Neill, H. S. C. & Hibberson, W. O. (1997). Experimental tests of low degree peridotite partial melt compositions: implications for the nature of anhydrous near-solidus peridotite melts at 1 GPa. *Earth and Planetary Science Letters* **152**, 149–162.

Falloon, T. J., Green, D. H., Danyushevsky, L. V. & Faul, U. H. (1999). Peridotite melting at 1·0 and 1·5 GPa: an experimental evaluation of techniques using diamond aggregates and mineral mixes for determination of near-solidus melts. *Journal of Petrology* **40**, 1343–1375.

Freund, R., Garfunkel, Z. & Zak, I. (1970). The shear along the Dead Sea Rift. *Philosophical Transactions of the Royal Society of London* **267**, 107–130.

Gallagher, K. & Hawkesworth, C. J. (1992). Dehydration melting and the generation of continental flood basalts. *Nature* **358**, 57–59.

Goldstein, S. L., O'Nions, R. K. & Hamilton, P. J. (1984). A Sm–Nd isotopic study of atmospheric dusts and particulates from major river systems. *Earth and Planetary Science Letters* **70**, 221–236.

Green, T. H., Blundy, J. D., Adam, J. & Yaxley, G. M. (2000). SIMS determination of trace element partition coefficients between garnet, clinopyroxene and hydrous basaltic liquids at 2–7·5 GPa and 1080–1200°C. *Lithos* **53**, 165–187.

Haase, K. M., Goldshmidt, B. & Garbe-Schönberg, C.-D. (2004). Petrogenesis of Tertiary continental intra-plate lavas from the Westerwald region, Germany. *Journal of Petrology* **45**, 883–905.

Hart, S. R. (1984). A large-scale isotope anomaly in the Southern Hemisphere mantle. *Nature* **309**, 753–757.

Hart, S. R. & Dunn, T. (1993). Experimental cpx melt partitioning of 24 trace elements. *Contributions to Mineralogy and Petrology* **113**, 1–8.

Harte, B., Hunter, R. H. & Kinny, P. D. (1993). Melt geometry, movement and crystallization, in relation to mantle dykes, veins and metasomatism. *Philosophical Transactions of the Royal Society of London, Series A* **342**, 1–21.

Hegner, E. & Pallister, J. S. (1989). Pb, Sr, and Nd isotopic characteristics of Tertiary Red Sea Rift volcanics from the central Saudi Arabian coastal plain. *Journal of Geophysical Research* **94**, 7749–7755.

Henjes-Kunst, F., Altherr, R. & Baumann, A. (1990). Evolution and composition of the lithospheric mantle underneath the western Arabian peninsula: constraints from Sr–Nd isotope systematics of mantle xenoliths. *Contributions to Mineralogy and Petrology* **105**, 460–472.

Hirose, K. (1997). Partial melt compositions of carbonated peridotite at 3 GPa and role of CO_2 in alkali-basalt magma generation. *Geophysical Research Letters* **24**, 2837–2840.

Hirose, K. & Kawamoto, T. (1995). Hydrous partial melting of lherzolite at 1 GPa—the effect of H_2O on the genesis of basaltic magmas. *Earth and Planetary Science Letters* **133**, 463–473.

Hirose, K. & Kushiro, I. (1993). Partial melting of dry peridotites at high pressures: determination of compositions of melts segregated from peridotite using aggregates of diamond. *Earth and Planetary Science Letters* **114**, 477–489.

Hirschmann, M. M. (2000). Mantle solidus: experimental constraints and the effects of peridotite composition. *Geochemistry, Geophysics, Geosystems* **1**, doi:10.1029/2000GC000070.

Hirschmann, M. M., Baker, M. B. & Stolper, E. M. (1998). The effect of alkalis on the silica content of mantle-derived melts. *Geochimica et Cosmochimica Acta* **62**, 883–902.

Hirschmann, M. M., Kogiso, T., Baker, M. B. & Stolper, E. M. (2003). Alkalic magmas generated by partial melting of garnet pyroxenite. *Geology* **31**, 481–484.

Hoernle, K., Zhang, Y.-S. & Graham, D. (1995). Seismic and geochemical evidence for large-scale mantle upwelling beneaththe eastern Atlantic and western and central Europe. *Nature* **374**, 34–39.

Hofmann, A. W., Jochum, K. P., Seufert, M. & White, W. M. (1986). Nb and Pb in oceanic basalts: new constraints on mantle evolution. *Earth and Planetary Science Letters* **79**, 33–45.

Humphreys, E. R. & Niu, Y. (2009). On the composition of ocean island basalts (OIB): The effects of lithospheric thickness variation and mantle metasomatism. *Lithos* **112**, 118–136.

Irvine, T. N. & Baragar, W. R. A. (1971). A guide to the geochemical classification of the common volcanic rocks. *Canadian Journal of Earth Sciences* **8**, 523–548.

Ismail, M., Delpech, G., Cottin, J. Y., Grégoire, M., Moine, B. N. & Bilal, A. (2008). Petrological and geochemical constraints on the composition of the lithospheric mantle beneath Syrian rift, northern part of the Arabian plate. In: Coltorti, M. & Grégoire, M. (eds) *Metasomatism in Oceanic and Continental Lithospheric Mantle. Geological Society, London, Special Publications* **293**, 223–251.

Jarrar, G., Stern, R. J., Saffarine, G. & Al-Zubi, H. (2003). Late- and post-orogenic Neoproterozoic intrusions of Jordan: implications for crustal growth in the northernmost segment of the East African Orogen. *Precambrian Research* **123**, 295–319.

Johnson, J. S., Gibson, S. A., Thompson, R. N. & Nowell, G. M. (2005). Volcanism in the Vitim Volcanic Field, Siberia: geochemical

evidence for a mantle plume beneath the Baikal Rift zone. *Journal of Petrology* **46**, 1309–1344.

Kaliwoda, M. (2004). Mantle xenoliths of the Harrat Uwayrid (Saudi Arabia): archives of compositional and thermal evolution of the lithospheric mantle in a passive continental margin setting, PhD thesis, Ruprecht-Karls-Universität, Heidelberg.

Kaliwoda, M., Altherr, R. & Meyer, H. P. (2007). Composition and thermal evolution of the lithospheric mantle beneath the Harrat Uwayrid, eastern flank of the Red Sea rift (Saudi Arabia). *Lithos* **99**, 105–120.

Katz, R. F., Spiegelman, M. & Langmuir, C. H. (2003). A new parameterization of hydrous mantle melting. *Geochemistry, Geophysics, Geosystems* **4**, doi:10.1029/2002gc000433.

Kelemen, P. B., Shimizu, N. & Dunn, T. (1993). Relative depletion of niobium in some arc magmas and the continental crust: partitioning of K, Nb, La and Ce during melt/rock reaction in the upper mantle. *Earth and Planetary Science Letters* **120**, 111–134.

Keskin, M. (2003). Magma generation by slab steepening and breakoff beneath a subduction–accretion complex: an alternative model for collision-related volcanism in Eastern Anatolia, Turkey. *Geophysical Research Letters* **30**, doi:10.1029/2003GL018019.

Keskin, M. (2007). Eastern Anatolia: a hot spot in a collision zone without a mantle plume. In: Foulger, G. R. & Jurdy, D. M. (eds) *Plates, Plumes, and Planetary Processes. Geological Society of America, Special Papers* **430**, 693–722.

Klein, E. M. & Langmuir, C. H. (1987). Global correlations of ocean ridge basalt chemistry with axial depth and crustal thickness. *Journal of Geophysical Research* **92**, 8089–8115.

Kogiso, T., Hirschmann, M. M. & Frost, D. J. (2003). High-pressure partial melting of garnet pyroxenite: possible mafic lithologies in the source of ocean island basalts. *Earth and Planetary Science Letters* **216**, 603–617.

Kogiso, T., Hirschmann, M. M. & Pertermann, M. (2004). High-pressure partial melting of mafic lithologies in the mantle. *Journal of Petrology* **45**, 2407–2422.

Krienitz, M.-S. (2004). The continental intraplate volcanism of Syria: rift-related or plume-induced, PhD Thesis, Christian-Albrechts-Universität, Kiel.

Krienitz, M.-S., Haase, K. M., Mezger, K., Eckardt, V. & Shaikh-Mashail, M. A. (2006). Magma genesis and crustal contamination of continental intraplate lavas in northwestern Syria. *Contributions to Mineralogy and Petrology* **151**, 698–716.

Krienitz, M.-S., Haase, K. M., Mezger, K. & Shaikh-Mashail, M. A. (2007). Magma genesis and mantle dynamics at the Harrat Ash Shamah volcanic field (southern Syria). *Journal of Petrology* **48**, 1513–1542.

Krienitz, M.-S., Haase, K. M., Mezger, K., van den Bogaard, P., Thiemann, V. & Shaikh-Mashail, M. A. (2009). Tectonic events, continental intraplate volcanism, and mantle plume activity in northern Arabia: constraints from geochemistry and Ar–Ar dating of Syrian lavas. *Geochemistry, Geophysics, Geosystems* **10**, doi:10.1029/2008GC002254.

Kushiro, I. (1996). Partial melting of a fertile peridotite at high pressure: an experimental study using aggregates of diamond. In: Basu, A. & Hart, S. (eds) *Earth Processes: Reading the Isotope Code. Geophysical Monograph, American Geophysical Union* **95**, 109–122.

LaÏTourrette, T., Hervig, R. L. & Holloway, J. R. (1995). Trace element partitioning between amphibole, phlogopite, and basanite melt. *Earth and Planetary Science Letters* **135**, 13–30.

Le Maitre, R. W. (2002). *Igneous Rocks: a Classification and Glossary of Terms: Recommendations of International Union of Geological Sciences Subcommission on the Systematics of Igneous Rocks*. Cambridge: Cambridge University Press.

le Roex, A. P., Späth, A. & Zartman, R. E. (2001). Lithospheric thickness beneath the southern Kenya Rift: implications from basalt geochemistry. *Contributions to Mineralogy and Petrology* **142**, 89–106.

Liang, Q., Jing, H. & Grégoire, D. C. (2000). Determination of trace elements in granites by inductively coupled plasma mass spectrometry. *Talanta* **51**, 507–513.

Liang, X.-R., Wei, G.-J., Li, X.-H. & Liu, Y. (2003). Precise measurement of $^{143}Nd/^{144}Nd$ and Sm/Nd ratios using multiple-collectors inductively coupled plasma-mass spectrometer (MC-ICPMS). *Geochimica* **32**, 91–96 (in Chinese with English abstract).

Lorand, J.-P. & Gregoire, M. (2010). Petrogenesis of Fe–Ti oxides in amphibole-rich veins from the Lherz orogenic peridotite (Northeastern Pyrenees, France). *Contributions to Mineralogy and Petrology* **160**, 99–113.

Lucassen, F., Franz, G., Romer, R. L., Pudlo, D. & Dulski, P. (2008). Nd, Pb, and Sr isotope composition of Late Mesozoic to Quaternary intra-plate magmatism in NE Africa (Sudan, Egypt): high-μ signatures from the mantle lithosphere. *Contributions to Mineralogy and Petrology* **156**, 765–784.

Lustrino, M. & Dallai, L. (2003). On the origin of EM-I end-member. *Neues Jahrbuch für Mineralogie, Abhandlungen* **179**, 85–100.

Lustrino, M. & Sharkov, E. (2006). Neogene volcanic activity of western Syria and its relationship with Arabian plate kinematics. *Journal of Geodynamics* **42**, 115–139.

Matmon, A. S., Wdowinski, S. & Hall, J. K. (2003). Morphological and structural relations in the Galilee extensional domain, Northern Israel. *Tectonophysics* **371**, 321–341.

McDonough, W. F. & Sun, S. S. (1995). The composition of the Earth. *Chemical Geology* **120**, 223–253.

McGuire, A. V. (1988). The mantle beneath the Red Sea margin: xenoliths from western Saudi Arabia. *Tectonophysics* **150**, 101–119.

McKenzie, D. (1989). Some remarks on the movement of small melt fractions in the mantle. *Earth and Planetary Science Letters* **95**, 53–72.

McKenzie, D. & Bickle, M. J. (1988). The volume and composition of melt generated by extension of the lithosphere. *Journal of Petrology* **29**, 625–679.

McKenzie, D. & O'Nions, R. K. (1991). Partial melt distributions from inversion of rare earth element concentrations. *Journal of Petrology* **32**, 1021–1091.

Mengel, K. & Green, D. H. (1989). Stability of amphibole and phlogopite in metasomatized peridotite under water-saturated and water-undersaturated conditions. In: Ross, J. (ed.) *Kimberlites and Related Rocks: Proceedings of the Fourth International Kimberlite Conference*. Perth: Geological Society of Australia, pp. 571–581.

Morimoto, N. (1989). Nomenclature of pyroxenes. *Canadian Mineralogist* **27**, 143–156.

Morris, E. M. & Pasteris, J. D. (eds) (1987). *Mantle Metasomatism and Alkaline Magmatism. Geological Society of America, Special Papers* **215**.

Nasir, S. & Rollinson, H. (2009). The nature of the subcontinental lithospheric mantle beneath the Arabian Shield: mantle xenoliths from southern Syria. *Precambrian Research* **172**, 323–333.

Nasir, S. & Safarjalani, A. (2000). Lithospheric petrology beneath the northern part of the Arabian Plate in Syria: evidence from xenoliths in alkali basalts. *Journal of African Earth Sciences* **30**, 149–168.

Niida, K. & Green, D. H. (1999). Stability and chemical composition of pargasitic amphibole in MORB pyrolite under upper mantle conditions. *Contributions to Mineralogy and Petrology* **135**, 18–40.

Niu, Y. (2008). The origin of alkaline lavas. *Science* **320**, 883–884.

Niu, Y. (2009). Some basic concepts and problems on the petrogenesis of intra-plate ocean island basalts. *Chinese Science Bulletin* **54**, 4148–4160.

Niu, Y. & O'Hara, M. J. (2003). Origin of ocean island basalts: a new perspective from petrology, geochemistry, and mineral physics

considerations. *Journal of Geophysical Research* **108**, 2209, doi:10.1029/2002JB002048.

Park, Y., Nyblade, A. A., Rodgers, A. J. & Al-Amri, A. (2007). Upper mantle structure beneath the Arabian Peninsula and northern Red Sea from teleseismic body wave tomography: implications for the origin of Cenozoic uplift and volcanism in the Arabian Shield. *Geochemistry, Geophysics, Geosystems* **8**, Q06021, doi:10.1029/2006GC001566.

Pertermann, M. & Hirschmann, M. M. (2003). Anhydrous partial melting experiments on MORB-like eclogite: phase relations, phase compositions and mineral–melt partitioning of major elements at 2–3 GPa. *Journal of Petrology* **44**, 2173–2201.

Pik, R., Deniel, C., Coulon, C., Yirgu, G. & Marty, B. (1999). Isotopic and trace element signatures of Ethiopian flood basalts: evidence for plume–lithosphere interactions. *Geochimica et Cosmochimica Acta* **63**, 2263–2279.

Pilet, S., Hernandez, J., Bussy, F. & Sylvester, P. J. (2004). Short-term metasomatic control of Nb/Th ratios in the mantle sources of intraplate basalts. *Geology* **32**, 113–116.

Pilet, S., Baker, M. B. & Stolper, E. M. (2007). Recycled metasomatised lithosphere as a source of alkaline OIBs. *EOS Transactions, American Geophysical Union* **88(52)**, Fall Meeting Supplement, Abstract V44B-06.

Pilet, S., Baker, M. B. & Stolper, E. M. (2008). Metasomatized lithosphere and the origin of alkaline lavas. *Science* **320**, 916–919.

Pilet, S., Ulmer, P. & Villiger, S. (2010). Liquid line of descent of a basanitic liquid at 1·5 Gpa: constraints on the formation of metasomatic veins. *Contributions to Mineralogy and Petrology* **159**, 621–643.

Prytulak, J. & Elliott, T. (2007). TiO_2 enrichment in ocean island basalts. *Earth and Planetary Science Letters* **263**, 388–403.

Quennell, A. M. (1984). The Western Arabia rift system. In: Dixon, J. E. & Robertson, H. F. (eds) *The Geological Evolution of the Eastern Mediterranean. Geological Society, London, Special Publications* **17**, 775–788.

Robinson, J. A. C., Wood, B. J. & Blundy, J. D. (1998). The beginning of melting of fertile and depleted peridotite at 1·5 GPa. *Earth and Planetary Science Letters* **155**, 97–111.

Roeder, P. L. & Emslie, R. F. (1970). Olivine–liquid equilibrium. *Contributions to Mineralogy and Petrology* **29**, 275–289.

Rudnick, R. L. & Fountain, D. M. (1995). Nature and composition of the continental crust: a lower crustal perspective. *Reviews of Geophysics* **33**, 267–309.

Rudnick, R. L. & Gao, S. (2003). Composition of the continental crust. In: Rudnick, R. L. (ed.) *The Crust. Treatise on Geochemistry 3*. Oxford: Elsevier–Pergamon, pp. 1–64.

Searle, M., Chung, S.-L. & Lo, C.-H. (2010). Geological offsets and age constraints along the northern Dead Sea fault, Syria. *Journal of the Geological Society, London* **167**, 1001–1008.

Sengör, A. M. C., Ozeren, S., Genc, T. & Zor, E. (2003). East Anatolian high plateau as a mantle-supported, north–south shortened domal structure. *Geophysical Research Letters* **30**, doi:10.1029/2003GL017858.

Sharkov, E. V., Chernyshev, I. V., Devyatkin, E. V., Dodonov, A. E., Ivanenko, V. V., Karpenko, M. I., Leonov, Y. G., Novikov, V. M., Hanna, S. & Khatib, K. (1994). Geochronology of Late Cenozoic basalts in western Syria. *Petrology* **2**, 439–448.

Sharkov, E. V., Snyder, G. A., Taylor, L. A., Laz'ko, E. E., Jerde, E. & Hanna, S. (1996). Geochemical peculiarities of the asthenosphere beneath the Arabian plate: evidence from mantle xenoliths of the Quaternary Tell-Danun volcano (Syrian–Jordan Plateau, southern Syria). *Geochemistry International* **34**, 737–752.

Sharkov, E. V., Chernyshev, I. V., Devyatkin, E. V., Dodonov, A. E., Ivanenko, V. V., Karpenko, M. I., Leonov, Y. G., Novikov, V. M., Hanna, S. & Khatib, K. (1998). New data on the geochronology of upper Cenozoic plateau basalts from the northeastern periphery of the Red Sea Rift area (northern Syria). *Doklady Earth Sciences* **358**, 19–22.

Shaw, D. M. (1970). Trace element fractionation during anatexis. *Geochimica et Cosmochimica Acta* **34**, 237–243.

Shaw, J. E., Baker, J. A., Menzies, M. A., Thirlwall, M. F. & Ibrahim, K. M. (2003). Petrogenesis of the largest intraplate volcanic field on the Arabian Plate (Jordan): a mixed lithosphere–asthenosphere source activated by lithospheric extension. *Journal of Petrology* **44**, 1657–1679.

Shaw, J. E., Baker, J. A., Kent, A. J. R., Ibrahim, K. M. & Menzies, M. A. (2007). The geochemistry of the Arabian lithospheric mantle—a source for intraplate volcanism? *Journal of Petrology* **48**, 1495–1512.

Sleep, N. H. (2008). Channeling at the base of the lithosphere during the lateral flow of plume material beneath flow line hot spots. *Geochemistry, Geophysics, Geosystems* **9**, doi:10.1029/2008gc002090.

Späth, A., le Roex, A. P. & Opiyo-Akech, N. (2001). Plume–lithosphere interaction and the origin of continental rift-related alkaline volcanism—the Chyulu Hills volcanic province, southern Kenya. *Journal of Petrology* **42**, 765–787.

Sprung, P., Schuth, S., Münker, C. & Hoke, L. (2007). Intraplate volcanism in New Zealand: the role of fossil plume material and variable lithospheric properties. *Contributions to Mineralogy and Petrology* **153**, 669–687.

Stein, M. & Goldstein, S. L. (1996). From plume head to continental lithosphere in the Arabian–Nubian shield. *Nature* **382**, 773–778.

Stein, M. & Hofmann, A. W. (1992). Fossil plume head beneath the Arabian lithosphere? *Earth and Planetary Science Letters* **114**, 193–209.

Stein, M., Garfunkel, Z. & Jagoutz, E. (1993). Chronothermometry of peridotitic and pyroxenitic xenoliths: implications for the thermal evolution of the Arabian lithosphere. *Geochimica et Cosmochimica Acta* **57**, 1325–1337.

Stein, M., Navon, O. & Kessel, R. (1997). Chromatographic metasomatism of the Arabian–Nubian lithosphere. *Earth and Planetary Science Letters* **152**, 75–91.

Stolper, E. & Asimow, P. (2007). Insights into mantle melting from graphical analysis of one-component systems. *American Journal of Science* **307**, 1051–1139.

Sun, S. S. & McDonough, W. F. (1989). Chemical and isotopic systematics of oceanic basalts: implications for mantle composition and processes. In: Saunders, A. D. & Norry, M. J. (eds) *Magmatism in the Ocean Basins. Geological Society, London, Special Publications* **42**, 313–345.

Takahashi, E., Shimazaki, T., Tsuzaki, Y. & Yoshida, H. (1993). Melting study of a peridotite KLB-1 to 6·5 GPa, and the origin of basaltic magmas. *Philosophical Transactions of the Royal Society of London. Series A* **342**, 105–120.

Tanaka, T., Togashi, S., Kamioka, H., Amakawa, H., Kagami, H., Hamamoto, T., Yuhara, M., Orihashi, Y., Yoneda, S., Shimizu, H., Kunimaru, T., Takahashi, K., Yanagi, T., Nakano, T., Fujimaki, H., Shinjo, R., Asahara, Y., Tanimizu, M. & Dragusanu, C. (2000). JNdi-1: a neodymium isotopic reference in consistency with LaJolla neodymium. *Chemical Geology* **168**, 279–281.

Taylor, S. R. & McLennan, S. M. (1995). The geochemical evolution of the continental crust. *Reviews of Geophysics* **33**, 241–265.

Thompson, R. N. & Gibson, S. A. (2000). Transient high temperatures in mantle plume heads inferred from magnesian olivines in Phanerozoic picrites. *Nature* **407**, 502–506.

Thompson, R. N., Ottley, C. J., Smith, P. M., Pearson, D. G., Dickin, A. P., Morrison, M. A., Leat, P. T. & Gibson, S. A. (2005). Source of the Quaternary alkalic basalts, picrites and basanites of

the Potrillo Volcanic Field, New Mexico, USA: lithosphere or convecting mantle? *Journal of Petrology* **46**, 1603–1643.

Tiepolo, M., Vannucci, R., Bottazzi, P., Oberti, R., Zanetti, A. & Foley, S. F. (2000). Partitioning of rare earth elements, Y, Th, U, and Pb between pargasite, kaersutite, and basanite to trachyte melts: Implications for percolated and veined mantle. *Geochemistry, Geophysics, Geosystems* **1**, doi:10.1029/2000GC000064.

Tiepolo, M., Oberti, R., Zanetti, A., Vannucci, R. & Foley, S. F. (2007). Trace-element partitioning between amphibole and silicate melt. In: Hawthorne, F. C., Oberti, R., Della Ventura, G. & Mottana, A. (eds) *Amphiboles: Crystal Chemistry, Occurrence, and Health Issues. Mineralogical Society of America and Geochemical Society, Reviews in Mineralogy and Geochemistry* **67**, 417–451.

Todt, W., Cliff, R. A., Hanser, A. & Hofmann, A. W. (1993). Re-calibration of NBS lead standards using a $^{202}Pb + {}^{205}Pb$ double spike. *Terra Nova* **5**(Abstract Supplementary 1): 396.

Trifonov, V. G., Trubikhin, V. M., Adzhamyan, Z., Dzhallad, S., El' Khair, Y. & Ayed, K. (1991). Levant fault zone in northeast Syria. *Geotectonics* **25**, 145–154.

Tsuruta, K. & Takahashi, E. (1998). Melting study of an alkali basalt JB-1 up to 12·5 GPa: behavior of potassium in the deep mantle. *Physics of The Earth and Planetary Interiors* **107**, 119–130.

Turkmani, A. (2000). Model of the upper mantle beneath the south western region of Syria, deduced form the study of peridotite xenoliths. In: Youssef, E.-S. A. A. (ed.) *Proceedings of the 5th International Conference on the Geology of the Arab World*. Giza: Cairo University, pp. 167–200.

Turkmani, A. S. & Al-Shara'a, M. (2004). Mantle ultramafic xenoliths in alkaline magmas on the eastern part of Al-Ghab Depression (Syria): evidence of shallow upper mantle. *Middle East Research Center (MERC), Ain Shams University. Earth Science Series* **18**, 27–48.

van Westrenen, W., Blundy, J. D. & Wood, B. J. (2000). Effect of Fe^{2+} on garnet–melt trace element partitioning: experiments in FCMAS and quantification of crystal-chemical controls in natural systems. *Lithos* **53**, 191–203.

Volker, F., McCulloch, M. T. & Altherr, R. (1993). Submarine basalts from the Red Sea: new Pb, Sr, and Nd isotopic data. *Geophysical Research Letters* **20**, 927–930.

Walter, M. J. (1998). Melting of garnet peridotite and the origin of komatiite and depleted lithosphere. *Journal of Petrology* **39**, 29–60.

Wasylenki, L. E., Baker, M. B., Kent, A. J. R. & Stolper, E. M. (2003). Near-solidus melting of the shallow upper mantle: partial melting experiments on depleted peridotite. *Journal of Petrology* **44**, 1163–1191.

Weaver, B. L. & Tarney, J. (1984). Empirical approach to estimating the composition of the continental crust. *Nature* **310**, 575–577.

Wedepohl, K. H. (1995). The composition of the continental crust. *Geochimica et Cosmochimica Acta* **59**, 1217–1239.

Wei, G.-J., Liang, X.-R., Li, X.-H. & Liu, Y. (2002). Precise measurement of Sr isotopic composition of liquid and solid base using (LP) MC-ICPMS. *Geochimica* **31**, 295–299 (in Chinese with English abstract).

Weinstein, Y., Navon, O., Altherr, R. & Stein, M. (2006). The role of lithospheric mantle heterogeneity in the generation of Plio-Pleistocene alkali basaltic suites from NW Harrat Ash Shaam (Israel). *Journal of Petrology* **47**, 1017–1050.

Wilson, M. & Patterson, R. (2001). Intraplate magmatism related to short-wavelength convective instabilities in the upper mantle: evidence from the Tertiary–Quaternary volcanic province of western and central Europe. In: Ernst, R. E. & Buchan, K. L. (eds) *Mantle Plumes: Their Identification Through Time. Geological Society of America, Special Papers* **352**, 37–58.

Witt-Eickschen, G., Seck, H. A., Mezger, K., Eggins, S. M. & Altherr, R. (2003). Lithospheric mantle evolution beneath the Eifel (Germany): constraints from Sr–Nd–Pb isotopes and trace element abundances in spinel peridotite and pyroxenite xenoliths. *Journal of Petrology* **44**, 1077–1095.

Workman, R. K. & Hart, S. R. (2005). Major and trace element composition of the depleted MORB mantle (DMM). *Earth and Planetary Science Letters* **231**, 53–72.

Workman, R. K., Hart, S. R., Jackson, M., Regelous, M., Farley, K. A., Blusztajn, J., Kurz, M. & Staudigel, H. (2004). Recycled metasomatized lithosphere as the origin of the Enriched Mantle II (EM2) end-member: Evidence from the Samoan Volcanic Chain. *Geochemistry, Geophysics, Geosystems* doi:10.1029/2003gc000623.

Wörner, G., Zindler, A., Staudigel, H. & Schmincke, H. U. (1986). Sr, Nd and Pb isotope geochemistry of Tertiary and Quaternary volcanics from West Germany. *Earth and Planetary Science Letters* **79**, 107–119.

Zou, H. (2007). *Quantitative Geochemistry*. London: Imperial College Press.

APPENDIX A: ANALYTICAL METHODS

Representative, fresh lava samples (and one volcanic bomb), screened by petrographic examination, were selected for whole-rock geochemical analysis. Any weathered surfaces and calcite amygdales were removed before analysis.

Loss on ignition (LOI) and abundances of major and trace elements were determined at the University of Hong Kong. Major elements, Ni and Cu were analysed by wavelength-dispersive X-ray fluorescence spectrometry (XRF) on fused glass discs and pressed powder pellets, respectively, using a Philips PW2400 spectrometer. Trace element, including rare earth element (REE), analysis was performed by inductively coupled plasma mass spectrometry (ICP-MS) using a VG Plasma-Quad ExCell system after a 12 h digestion using a HF–HNO_3 mixture in high-pressure bombs (Liang *et al.*, 2000), with Rh as an internal standard. The quality of analysis by XRF and ICP-MS was assessed using procedural blanks (only for ICP-MS), international reference materials and repeated analyses of the same samples. Instrumental drift was monitored by routinely analysing the same international reference materials between approximately every 10 samples, and molecular oxide interferences (e.g. Ba–Pr–Eu–Gd in ICP-MS) were monitored by spiked solutions of known concentrations (e.g. Ba and Pr). The 'within-run' repeatability of the XRF and ICP-MS measurements, as monitored by replicate analyses, was generally better than 2% for most major elements, 1% for Ni, and 5% for Cu and most other trace elements. The long-term reproducibility of these methods, as monitored by analysed international reference standards in different runs (days), was generally better than 5% for most major elements and 10% for most trace elements. Data for the international reference

standards AGV-2, BHVO-2 and GSR-3 (Table 1) are in good agreement with the published recommended values.

Whole-rock Sr–Nd–Pb isotopic compositions were measured at the Key Laboratory of Isotope Geochronology and Geochemistry, Guangzhou Institute of Geochemistry, Chinese Academy of Sciences (GIG-CAS). Before acid digestion, several samples (S10-05, S68-05, S103-05 and S105-05) were leached with 6N HCl for 5 min and then carefully rinsed a number of times with high-purity deionized water. For Sr and Nd isotopic analyses, samples (~100 mg) were dissolved in Teflon beakers using a HF–HNO_3 mixture for 14 days at ~80°C. Extraction of Sr and REE was performed by conventional cation exchange chromatography with HCl as a solvent; further extraction of Nd was achieved on HDEHP columns. The techniques have been described by Wei *et al.* (2002) and Liang *et al.* (2003). The analyses were carried out by multi-collector ICP-MS using a Micromass IsoProbe system and the measured $^{87}Sr/^{86}Sr$ and $^{143}Nd/^{144}Nd$ ratios were corrected for mass fractionation relative to $^{86}Sr/^{88}Sr = 0{\cdot}1194$ and $^{146}Nd/^{144}Nd = 0{\cdot}7219$, respectively. The NBS-987 and the Shin Etsu JNDi-1 reference materials ($n = 16$) determined during the period of data acquisition gave average values of $^{87}Sr/^{86}Sr = 0{\cdot}71025 \pm 7$ (2σ) and $^{143}Nd/^{144}Nd = 0{\cdot}512106 \pm 10$ (2σ), respectively. Nd isotope data were normalized to a value of 0·512115 for the Shin Estu JNdi-1 reference material (Tanaka *et al.*, 2000). For Pb isotopic analyses, separation of Pb was accomplished by the anion exchange method in HCl–Br columns. The analyses were performed by thermal ionization mass spectrometry (TIMS) on a VG-354 mass spectrometer. Standard runs of NBS-981 gave $^{206}Pb/^{204}Pb = 16{\cdot}933 \pm 0{\cdot}018$, $^{207}Pb/^{204}Pb = 15{\cdot}491 \pm 0{\cdot}015$ and $^{208}Pb/^{204}Pb = 36{\cdot}673 \pm 0{\cdot}038$ (2σ), yielding correction factors of 0·99995, 0·99964 and 1·00291, respectively, relative to Todt *et al.* (1993).

Major element compositions for minerals in the volcanic rocks were obtained at GIG-CAS (the majority; those tagged with 'GZ' in their laboratory numbers) and at the Department of Earth Sciences, Oxford University (for small numbers of analyses). At Guangzhou, these were determined using a JEOL JXA-8100 Superprobe equipped with five wavelength-dispersive spectrometers. Operating parameters were 15 kV accelerating voltage, 20 nA current, ~1 μm beam diameter and 10–30s counting time (30 s for Ca; 12 s for K; 10 s for Na; 20 s for all other elements). Olivine (Si, Fe, Mg, Ni), rutile (Ti), albite (Al, Na), K-feldspar (K), diopside (Ca), bustamite (Mn) and Cr-oxide (Cr) were used for calibration, and the final results were reduced by a ZAF correction program. At Oxford, mineral compositions were determined by a JEOL-840A SEM equipped with an Oxford Instruments Isis 300 energy-dispersive analytical system (EDS). Operating conditions were 100 s live counting time, 20 kV accelerating voltage and 6 nA beam current. Standardization and matrix corrections were performed as at GIG-CAS. For mineral grains that were analysed at both places, the results agree very well.

APPENDIX B: SUMMARY OF PREVIOUSLY PUBLISHED DATA

In this study, data, especially isotopic data, from several previously published studies (Abdel-Rahman & Nassar, 2004; Lustrino & Sharkov, 2006; Krienitz *et al.*, 2009) for the N-DSFS volcanic fields were used to augment our new data. Because of the unavailability of petrographic information for these samples, LOI was used to estimate the degree of alteration in these samples. Initial screening revealed that some samples with high LOI (>4 wt %) were characterized by radiogenic $^{87}Sr/^{86}Sr$, attesting to the potential influence of low-temperature alteration. As such, all the published data used in this study were filtered for LOI ≤ 2 wt %. Moreover, analyses of Th and U by Abdel-Rahman & Nassar (2004; by XRF) and Pb by Lustrino & Sharkov (2006) may be problematic and were excluded from the database. In places, where Ce/Pb was used to assess the effects of crustal contamination, Nb/U was used instead for Lustrino & Sharkov's (2006) samples [considering that $Nb/U = 47 \pm 10$ for oceanic basalts (Hofmann *et al.*, 1986)].